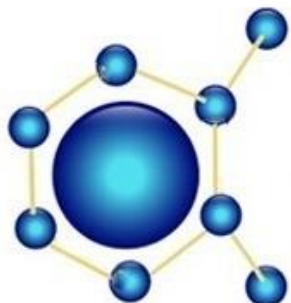




**SETCOR**  
Conferences & Exhibitions



3rd Edition

**S M S**

Smart Materials and Surfaces

**EUROPE 2017**  
Conference

**26 - 28 April 2017 | Paris - France**

and

**EUROPEAN GRAPHENE FORUM**  
**EGF 2017**



**April 26 – 28, 2017 | Paris - France**

**Joint International Conferences**  
**Proceedings**

# Tailoring of moisture management PLA fibers: Application of temperature and pH responsive nanogel

D. Štular<sup>1</sup>, B. Tomšič<sup>1\*</sup>, B. Simončič<sup>1</sup>, I. Jerman<sup>2</sup>, M. Mihelčič<sup>2</sup>

<sup>1</sup>University of Ljubljana, Faculty of Natural Sciences and Engineering, Department of Textiles, Graphic Arts and Design, Aškerčeva 12, 1000 Ljubljana, Slovenia, danaja.stular@ntf.uni-lj.si

<sup>2</sup>National Institute of Chemistry, Hajdrihova ulica 19, 1000 Ljubljana, Slovenia

## Abstract

In this research, smart stimuli responsive fabric was tailored by incorporation of temperature and pH responsive nanogel based on poly(N-isopropylacrylamide) (poly-NiPAAm) and chitosan (PNCS nanogel). Nanogel with average shrunken particle size of 76 nm was synthesized and applied onto poly(lactic acid) (PLA) fabric by pad-dry-cure procedure. Stimuli responsive properties of the nanogel were assessed before and after its deposition to the PLA fibres by using dynamic light scattering (DLS), water uptake (*WU*), moisture content (*MC*) and water vapour transition rate (*WVTR*) measurements, while thin-layer wicking (TLW) method was used to characterise the hydrophilicity and porosity of the treated sample. Swelling of the nanogel particles was slightly hindered after the application of stimuli responsive coating to the PLA fibres, due to the nano sized film like arrangement, which covered entire fibres surface, thus impairing full swelling of the nanogel particles. Nevertheless, PNCS nanogel coated fabric exhibited temperature as well as pH responsive activity, namely it absorbed and restrained moisture at temperatures and pH below 32°C and 6.5 respectively, and expelled moisture when both stimuli increased. Consequently, improved moisture management properties were achieved. Such intelligent textile material shows great potential for the use in the medical field, as smart wound dressing material with controlled moisture management, whereas PNCS nanogel can be exploit as a carrier of different active substances, which could get released from its structure only on demand, i.e. at conditions required.

**Keywords:** intelligent textiles, stimuli-responsive nanogel, poly-NiPAAm, chitosan, PLA fibres, thermoregulation

## 1. Introduction

The incorporation of thin layer surface modifying system is one of the innovative strategies for tailoring “smart” textiles which have the ability of pro-active moisture management and thus thermoregulation properties by sensing and adapting to the physical condition of the wearer and the surrounding environment. For this purpose, stimuli responsive hydrogels in micro- or nano-sized particles can be used in textile functionalisation, which show great promise not only in development of apparel with increased wearing comfort, but also show the potential in medical textiles as smart wound dressings or as carriers of different active substances [1]. Accordingly, hydrogels responsive to the changes of temperature and pH are the most suitable, since both stimuli are of physiological meaning [2]. Nanogel composed of (poly-NiPAAm) and chitosan (PNCS nanogel) exhibits both temperature and pH responsiveness. Poly-NiPAAm is a temperature responsive polymer, with lower critical solution temperature (LCST) at approximately 32 °C, which is in the range of body temperature and temperature of the environment. Its rather complex polarity dictates coil conformation of the polymer when temperature is below LCST. Under such conditions, the polymer is soluble in water. When the temperature is risen above the LCST, the polymer undergoes coil to globe transition and hence, eliminates water from its structure. Furthermore, chitosan is a pH responsive biopolymer which can respond to changes in the pH of the surrounding medium. It possesses weak basic moieties in its structure, which protonate upon ionization, at pH below ~6.5. Due to the electrostatic repulsion, coiled chains extend and the volume of the polymer increases. On contrary, in basic media amino groups deprotonate and exhibit hydrophobic character [3-5]. Accordingly, PNCS nanogel swells and absorbs moisture when temperature is below 32 °C and pH below 6.5, and de-swells and expel the moisture when temperature and pH level rises. Such volume change can influence the porosity of the textile material, by regulating retention or release of body vapour. Since, when in their swollen phase, the hydrogel particles can absorb and restrain great amount of water, stimuli responsive

hydrogels can be exploited as a drug carrier, showing the ability of controlled release of active substances in the surrounding environment only at conditions required [6].

In the present research PNCS nanogel was applied to poly(lactic acid) (PLA) textile fabric, in order to impart proactive moisture management properties, with the potential use as smart wound managing material with controlled release of different active substances. Accordingly, among textile materials PLA fabric was chosen deliberately, due to its renewability and biocompatibility, which makes it readily used in medicine.

## 2. Experimental

### 2.1 Materials

In this study, 100 % PLA fabric Revolution® (M+N Textiles, Nederland) was used. For the preparation of the PNCS microgel, chitosan (Chitoclear, Primex, Iceland; DD = 95%;  $\eta = 159$  mPa), glacial acetic acid (Sigma Aldrich), N-isopropylacrylamide (NiPAAm) (Sigma Aldrich), N,N-methylenebisacrylamide (MBA) (Sigma Aldrich), ammonium persulfate (APS) (Sigma Aldrich), N'-tetramethylethylenediamine (TEMED) (Sigma Aldrich) and sodium dodecyl sulphate (SDS) with high purity (GE Healthcare Life Sciences) were used.

### 2.2 Synthesis of the PNCS nanogel and its application to PLA fabric

Free radical polymerisation was used to synthesize PNCS nanogel. Firstly, 0.32 g of APS and 0.1g of TEMED were dissolved in 60 mL of distilled water. Mixture was put in a flask, heated to 70 °C and degassed with nitrogen for 30 min, with constant stirring (420 rpm). Monomer solutions were prepared as follows: 4g of NiPAAm, 0,08 g of MBA and 1,58 g of 10 % SDS solution was dissolved in 100 mL of distilled water. Chitosan (0.57 g) was dissolved in 171 mL 0.6 w/w % solution of glacial acetic acid and stirred for 24 hours prior to use. Monomer solutions were added into the polymerisation mixture dropwise, in 2 h interval. Polymerisation proceeded for 4 hours at 70 °C, in nitrogen atmosphere at constant stirring. Nanogel reaction mixture was dialysed against bidistilled water using a Spectra/Por 4 membrane (Fisher Scientific) for 10 days to remove impurities and unreacted monomers. Water was changed daily. To apply PNCS nanogel onto PLA fabric, pad-dry application process with 80% wet pick-up was used, followed by air drying of the samples. The process was repeated two times. Untreated PLA sample was named UN\_PLA and the sample applied with PNCS nanogel was marked as PLA\_PNCS\_N.

### 2.3 Analysis and measurements

To determine particle size of dispersed nanogel, in correspondence with changes in temperature and pH prior to its application to PLA fabric was performed using dynamic light scattering (DLS) analysis, on Zetasizer Nano S (Malvern, UK), equipped with 4mW He-Ne laser operating at wavelength 633 nm and an avalanche photodiode. Particle size was determined at pH 7 and temperatures ranging from 20- to 40 °C in 5 °C intervals and at pH 3 and 10 at 20°C. 60  $\mu$ L of sample was used for each measurement, results are an average of 3 measurements.

Morphological changes of the studied PLA samples were determined using scanning electron microscope FE-SEM Zeiss SUPRA 35VP, at an accelerating voltage of 1 kV. Before observation, the samples were coated with Pd.

Temperature responsiveness of the samples was assessed by measuring moisture content using a Moisture analyser MLB-C (Kern & SOHN GmbH, Germany). Studied samples were pre-conditioned at 65 $\pm$ 2% relative humidity at 20 and 40°C for 24 h, before they were put in a moisture analyser and dried at 60 °C until the constant mass. Moisture content (*MC*) was determined by following equation:

$$MC = \left( \frac{m_0 - m_f}{m_0} \right) \times 100 [\%] \quad (1)$$

where  $m_0$  denote the initial mass of the pre-conditioned sample and  $m_f$  represents the final mass of the sample after drying. *MC* was reported as mean values of ten measurements.

Water vapour permeability was determined according to the standard method UNI 4818-26, and performed at 65% relative humidity either at 20 or at 40°C. Water vapour transmission rate (*WVTR*) was calculated by next equation:

$$WVTR = \left( \frac{\Delta m \times 24}{S \times t} \right) [\text{g/m}^2 \text{ day}] \quad (2)$$

where  $\Delta m$  corresponds to the change of mass [g],  $S$  is the testing area of the fabric sample [ $\text{m}^2$ ] (actual value  $76,68 \text{ mm}^2$ ) and  $t$  is the time of testing [h] (actual value 24 h). Results represent an average of seven measurements.

In order to evaluate dual, pH and temperature responsiveness of the PNCS microgel and nanogel, the samples of known mass were immersed in buffer solutions of different pH, i.e. 3, 6.5 and 10 for 30 minutes, at two different temperatures, i.e. 20 and 40 °C. Afterwards, the samples were taken from the buffers and weighed. Water uptake ( $WU$ ) was determined by following equation:

$$WU = \left( \frac{m_w - m_0}{m_0} \right) \times 100 [\%] \quad (3)$$

where  $m_w$  is the weight of the sample taking up water [g] and  $m_0$  is the initial weight of sample [g].  $WU$  are reported as mean values of ten measurements.

Thin-layer wicking (TLW) method [7-9] was used to verify the spreading of liquid driven into a sample by capillary forces. Prior to testing, the samples were either completely dried at 60°C for 4 hours or exposed to standard atmospheric conditions, i.e. 20 °C and 65 % for 24 hours. Firstly, distilled water was used as wicking liquid. Samples were placed between two glass plates, equipped with a ruler from which the water penetration distance at different penetration time could be determined. Samples prepared in this manner were placed on the edges of two cups with  $\sim 2^\circ$  inclination and the lower cup was filled with testing liquid. When sample came in contact with the liquid, osmotic pressure caused the latter to move through the fabric and time of the traveling was measured. Ten repetitions were made for each sample and the average value of  $x^2/t$  was obtained graphically from the slope ( $k$ ) of the plot of  $t$  versus  $x^2$ . Secondly, n-heptane was used as the testing liquid, in order to determine the apparent capillary radius  $R$  values. Samples were either dried on 60 °C for 4 hours and immediately placed over the saturated vapour of n-heptane for 24 hours at  $20 \pm 1^\circ\text{C}$  or preconditioned at standard atmosphere (20°C, 65% R.H.) for 24 hours prior to the measurements. This method allows us to assess the rate of the liquid penetration into a porous solid material, which can be calculated by the Washburn equation for the horizontal capillary:

$$\frac{x^2}{t} = \frac{R}{2\eta} \Delta G \quad (4)$$

where  $x$  is the penetration distance [cm],  $t$  is the time in which liquid reaches the distance  $x$  [s],  $R$  represents effective capillary radius of porous solid [m],  $\eta$  is the viscosity of the penetrating liquid [mPa·s] and  $\Delta G$  is the Gibbs free energy change accompanying the liquid penetration process ( $\text{mJ/m}^2$ ). A non-polar totally wetting liquid (n-heptane) was used since it has a low surface tension ( $\gamma_L = 20.1 \text{ mJ/m}^2$ ) of known viscosity  $\eta = 0.41 \text{ mPa s}$ . This kind of liquids were expected to spread spontaneously over the solid material, therefore the value of apparent capillary radius  $R$  of the porous solid material could be easily determined from the Washburn equation as in this case  $\cos\theta = 1$  and  $\Delta G = \gamma_L$  [8].

### 3. Results and discussion

#### 3.1. Hydrogel characterisation

DLS analysis was performed in order to investigate particle size in dependence of pH and temperature variation of the intermediate environment (fig. 1). Intensive volume change was obtained by the rise of pH (Fig. 1a), since particles of 663 nm in size were determined at pH 3, while their size decreased down to 76 nm at pH 10. Besides, a broad LCST, ranging from 25–40 °C was recorded, when observing de-swelling of the hydrogel particles with the temperature rise (Fig. 2b).

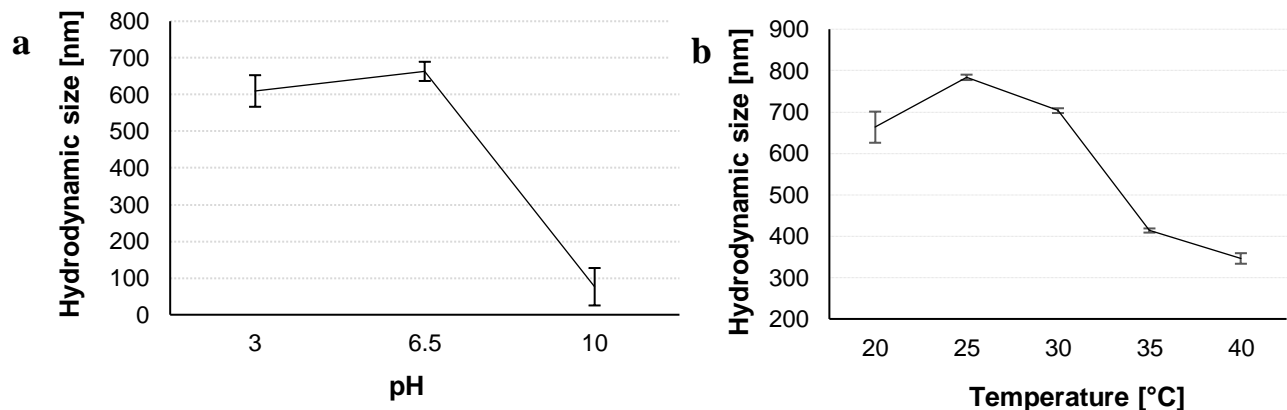


**Fig. 1:** Hydrodynamic diameter of PNCS nanogel particles as a function of pH variation at 20 °C (a) and temperature variation at neutral pH (b).

### 3.2. Morphological and chemical properties

Morphological changes of the studied samples were determined by SEM images, shown in Fig. 2. Uneven surface of untreated PLA fibres with cracks and impurities can be observed (Fig. 2a), while the application of the PNCS nanogel formed a continuous film, which covered and smoothed the fibre surface (Fig. 2b).

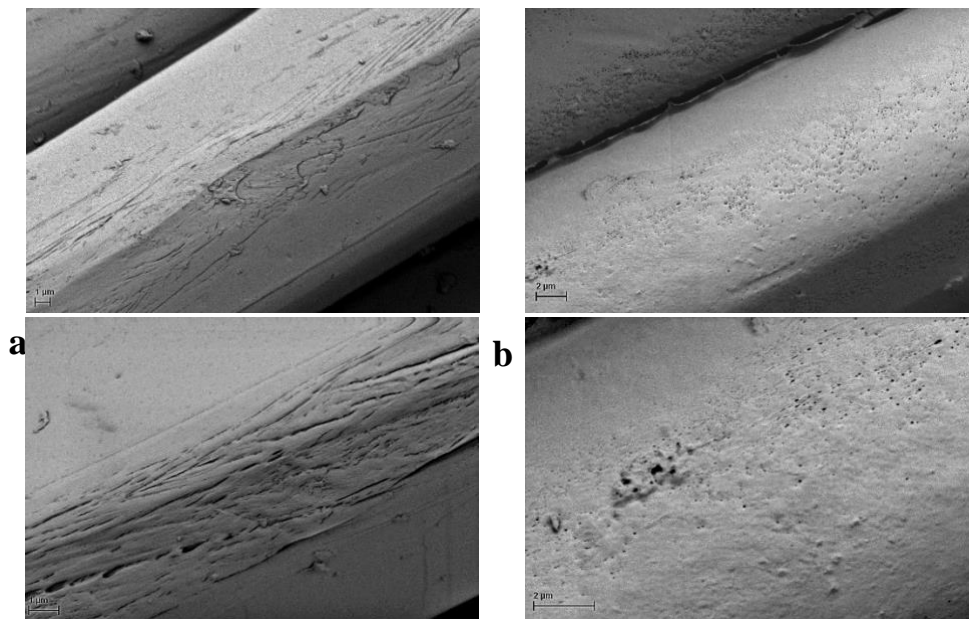


**Fig. 2:** Scanning electron microscope images of UN\_PLA (a) and, PLA\_PNCS\_N (b), recorded with a magnification of 10,000x (upper) and 20,000x (lower).

### 3.4. Temperature responsiveness

To study the temperature responsiveness of PLA\_PNCS\_N sample, moisture content (*MC*) and water vapour transition rate (*WVTR*) were determined (Fig. 3). Treated sample, preconditioned at 20°C, reflected 4.5% higher *MC* compared to UN\_PLA sample (Fig. 3a). At this conditions PNCS nanogel was in its swollen state, thus absorbing moisture from the surrounding environment. With the rise of preconditioning temperature up to 40°C, the hydrophobic character of poly-NiPAAm prevailed and phase change of PNCS nanogel occurred. PNCS nanogel collapsed and expelled water, which reflected in 28.0% decrease of *MC* compared to UN\_PLA sample. Accordingly, *WVTR* measurement (Fig. 3b) showed slightly higher water vapour retention of the CO\_PNCS\_N in comparison to

UN\_PLA sample at room temperature and 10.5% higher water vapour passage at 40°C. When compared *MC* and *WVTR* results, in both cases much higher differences between UN\_PLA and PLA\_PNCS\_N were obtained at conditions which dictates de-swelling of the PNCS nanogel. Most likely, the reason lies in the distribution of applied nanogel on the fibre surface. Namely, due to the film-like distribution on the fibre surface, swelling of the nanoparticles was restricted at 20°C, but positively influenced the release of moisture at 40°C, since water was not able to fully reach the surface of the PLA fibres. Thus we can assume, the hydrophobic character of the PNCS nanogel dominated the water-PLA interactions.

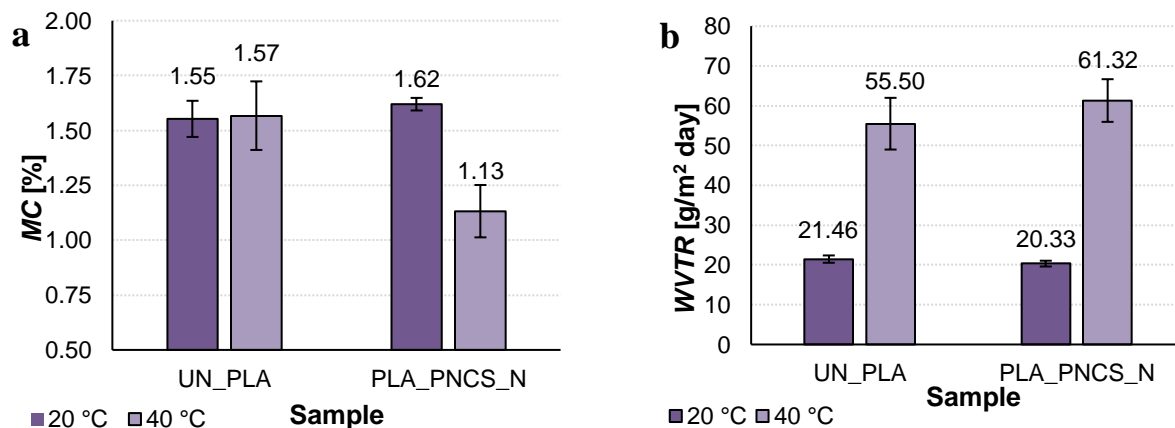


**Fig. 3:** Moisture content, *MC*, (a) and water vapour transition rate, *WVTR*, (b) of the studied samples after 24-hour preconditioning at 20°C or 40°C and 65±2%.

### 3.5. Temperature and pH responsiveness

*WU* measurement was used to determine dual temperature and pH responsiveness, granted by poly-NiPAAm and chitosan. It can be seen from Fig. 4 that application of PNCS microgel to the PLA fabric reflected in its temperature and pH responsiveness, since PLA\_PNCS\_N demonstrated greater differences among studied conditions compared to the untreated sample. Accordingly, the highest *WU* was determined at 20°C and pH 3, when both monomers in hydrogel structure are in hydrophilic state. On contrary when, poly-NiPAAm and chitosan are in collapsed, dehydrated state (i.e. 40 °C and pH 10), the sample PLA\_PNCS\_N showed the lowest *WU* and thus the opposite behaviour of the untreated sample UN\_PLA. From the results it can be also inferred, that temperature variations had greater impact on swelling/de-swelling ability of the PNCS nanogel than did the variation of the pH. Namely, much higher *WU* was obtained at 20 °C and pH 10, i.e. when poly-NiPAAm is bounding water and tends to swell, and chitosan is negatively charged and dehydrated, compared to the *WU* at 40°C and pH 3, when poly-NIPAAm discharges water and chitosan is hydrophilic. Such behaviour was expected, since in the PNCS synthesis process, the ratio between poly-NiPAAm and chitosan was in favour to the temperature responsive poly-NiPAAm.

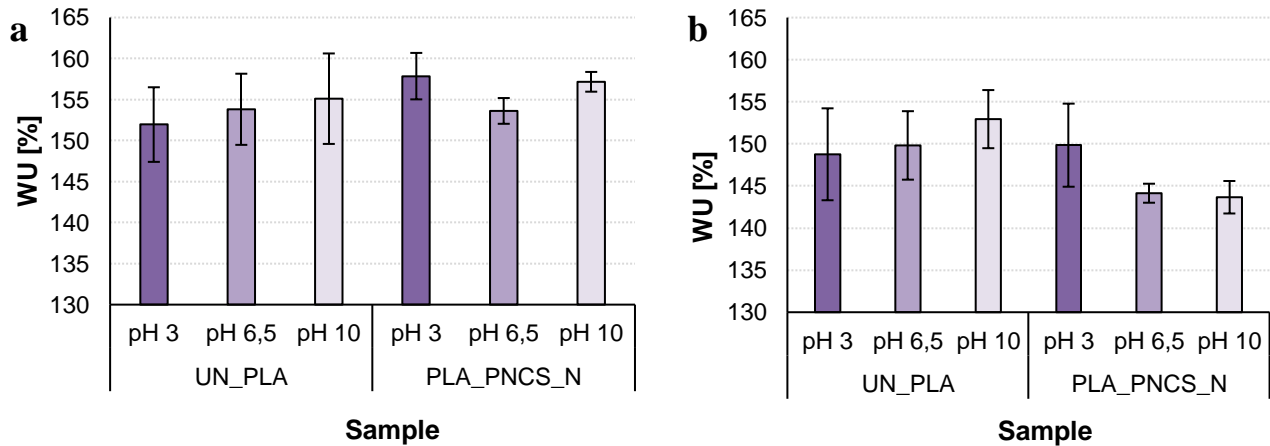


**Fig. 4:** Water uptake, *WU*, of the studied samples after being immersed in different buffer solutions preheated to 20°C (a) and 40°C (b).

### 3.6. Thin layer wicking

Hydrophilicity of the responsive coating at room temperature was further examined with the use of thin layer wicking (TLW) method, in order to study the rate of liquid spreading through the sample as a consequence of capillary forces, since moisture is the driving force of the nanogel responsiveness. It can be predicted that the speed of liquid penetration is based on the mechanism of liquid adsorption and rate of diffusion, since porous solids are thought of being constructed from bundle of capillary tubes through which the liquid could shift [7]. In Fig. 5 the penetration rate curves into both studied samples are shown, where water was used as wicking liquid, for dried samples containing no moisture and samples preconditioned at 65% R.H. for 24 hours. Overall, the presence of nanogel increased the hydrophilicity and thus wettability of the PLA, since penetration rate curves of PLA\_PNCS\_N sample demonstrated faster water penetration, compared to UN\_PLA sample, regardless of the preconditioning procedure.

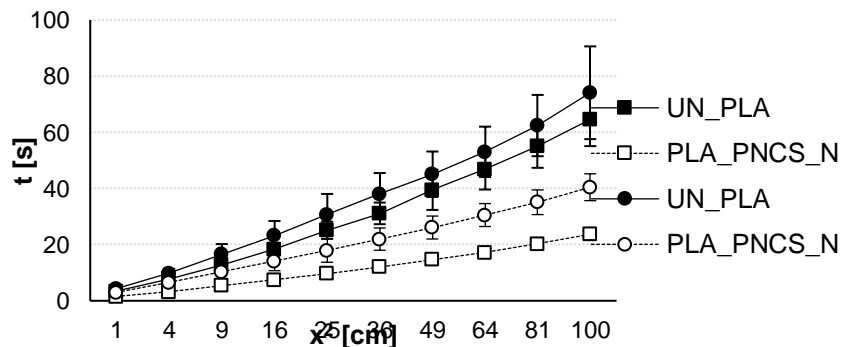


**Fig. 5:** Water penetration rate curves obtained by the thin-layer wicking measurements on absolutely dry PLA fabric samples (○) and samples preconditioned in standard atmosphere of 65% R.H. and 20°C for 24 h (□).

Subsequent, n-heptane was used as the wicking liquid, and apparent capillary radius (*R*) of the samples, which gives the information about the fabric porosity, was determined. Namely, *R* is related to the average value of the pore size (i.e. intra- and inter-yarns pores) and pore distribution in the PLA fabric [7]. As seen from Table 1 the average pore size increased after the application of the PNCS nanogel in comparison to the untreated UN\_PLA sample, indicating that the film-like distribution of the PNCS nanogel partially closed the porous system within the filaments in the yarn, thus influencing decreased contribution of the smallest pores to the *R* value. After the exposure to the standard atmospheric conditions *R* value of the untreated UN\_PLA sample slightly increased, while significant decrease was

observed for the PLA\_PNCS\_N sample, indicating swelling of the PNCS nanogel in the humid atmosphere as a result of water absorption.

Table 1: The slope ( $k$ ) and the apparent capillary radius ( $R$ ) of the studied PLA samples, obtained from the TLW measurements with n-heptane as the thin-layer wicking liquid; A - samples previously dried and saturated with n-heptane, B – samples preconditioned in standard atmosphere (20°C, 65% R.H.).

Sample	A		B	
	k	$R \times 10^{-6}$ [m]	k	$R \times 10^{-6}$ [m]
UN_PLA	0,23	1,79	0,21	1,94
PLA_PNCS_N	0,08	4,93	0,1	3,89

#### 4. Conclusion

From the results obtained it can be concluded, that PNCS nanogel, with a particles size of 76 nm when in de-swollen state, formed a film-like layer on the fibre surface, imparting controlled moisture management properties triggered by the variation of temperature and pH. Accordingly, increased water absorption at temperatures lower than 32 °C and pH below 6.5, was obtained, which was expelled into the surrounding environment by the increase of both stimuli. Regardless of slightly hindered water absorption abilities, due to a film-like arrangement, contribution to hydrophilicity and variation of porous system of the PLA fabric at predetermined conditions was proven by a faster water absorption and decreased apparent capillary radius of the treated sample, ascribed to the swelling of the nanogel. Such novel textile material shows great promise for the use in medicinal purposes, as a smart wound dressing with controlled moisture management and pro-active release of active substances.

#### Acknowledgements

This work was supported by the Slovenian Research Agency—Slovenia (Program P2-0213, Infrastructural Centre RIC UL-NTF and a Grant for the Dr. Sc. student D. Š.).

#### References

1. S.K. Samal, M. Dash, P. Dubruel and S. Van Vlierberghe, “Smart polymer hydrogels: properties, synthesis and applications”. In *Smart Polymers and their Applications*, M.R. Aguilar De Armas and J.S. Román (Eds.), 2014, pp. 237-270, Cambridge: Woodhead Publishing.
2. D. Jocić, “Smart coatings for comfort in clothing”. In *Active coatings for Smart Textiles*, J. Hu (Ed.), 2016, pp. 331-354, Cambridge: Woodhead Publishing.
3. A. Kulkarni, A. Tournette, M.M.C.G. Warmoeskerken, D. Jocić. “Microgel-based surface modifying system for stimuli-responsive functional finishing of cotton”. *Carbohydrate Polymers*, 2010, vol. 82(4), pp. 1306–1314.
4. A. Tournette, N. De Geyter, D. Jocić, R. Morent, M.M.C.G. Warmoeskerken and C. Leys. “Incorporation Of Poly(N-Isopropylacrylamide)/Chitosan Microgel Onto Plasma Functionalized Cotton Fibre Surface,” *Colloids and Surfaces A: Physicochemical and Engineering Aspects*, 2009, vol. 352, pp. 126–135.
5. J. Hu, H. Meng, G. Li, S. Ibeke, “A review of stimuli-responsive polymers for smart textile applications,” *Smart Materials and Structures*, 2012, vol. 21(5).
6. D. Štular, I. Jerman, I. Naglič, B. Simončič and B. Tomšič, “Embedment of silver into temperature- and pH-responsive microgel for the development of smart textiles with simultaneous moisture management and controlled antimicrobial activities” *Carbohydrate Polymers*, 2017, vol. 159, pp. 161–170.
7. P. Križman Lavrič, B. Tomšič, B. Simončič, M.M.C.G. Warmoeskerken and D. Jocić. “Functionalization of cotton with poly-NiPAAm/chitosan microgel. Part II. Stimuli-responsive liquid management properties,” *Cellulose*, 2012, vol. 19, pp. 273–287.
8. E. Chibowski and F. González-Caballero. “Theory and practice of thin-layer wicking”, *Langmuir*, 1993, vol. 9, pp. 330-340.
9. B. Simončič and V. Rozman, “Wettability of cotton fabric by aqueous solutions of surfactants with different structures”. *Colloids and Surfaces A: Physicochem. Eng. Aspects*, 2007, vol. 292, pp. 236-245.

# Modeling of the thermo-mechanical behavior of a semi-crystalline thermoplastic shape memory polymer

R Bouaziz<sup>1,2</sup> F Roger<sup>1,2</sup> and K Prashantha<sup>1,2</sup>

<sup>1</sup> IMT Lille Douai, Institut Mines-Télécom, Polymers and Composites Technology & Mechanical Engineering Department, 941 rue Charles Bourseul, 59508 Douai, France

<sup>2</sup> Université de Lille, 59000 Lille, France

## Abstract:

The semi-crystalline thermoplastic shape memory polyurethane (TPU-SMPU) is a smart material which has the ability to return to its original shape after applying a large strain thermo-mechanical cycle (Figure 1) when it is stimulated by heating. This smart material has the advantage of recovering even after more than 100% of strain during several thermo-mechanical cycles. To explore the performance of a smart component in a mechanical system, it is mandatory to master the prediction of its behavior through a numerical model. In this paper, a constitutive model is proposed to describe its thermo-mechanical behavior and to predict the shape memory response. Uniaxial tensile tests at small strain rates were performed at 60°C in order to analyze the hyper-elastic response for each cycle. Relaxation tests were carried out at the end of the previous tensile loading to highlight the viscoelastic response during the shape memory cycle. These experimental data were, then, used in a curve-fitting algorithm employing least-squares optimization approach in order to identify the parameters of the proposed model. At last, the shape memory effect was investigated by means of free and constrained recovery experiments. The proposed model was then implemented into Comsol Multiphysics. It predicts quite well the experimental results in all cycles. In order to assess its predictability, this model was finally applied to the design of a 3D structure.

**Keywords:** semi-crystalline shape memory polyurethane, constitutive model, thermo-mechanical cycle, large deformation.

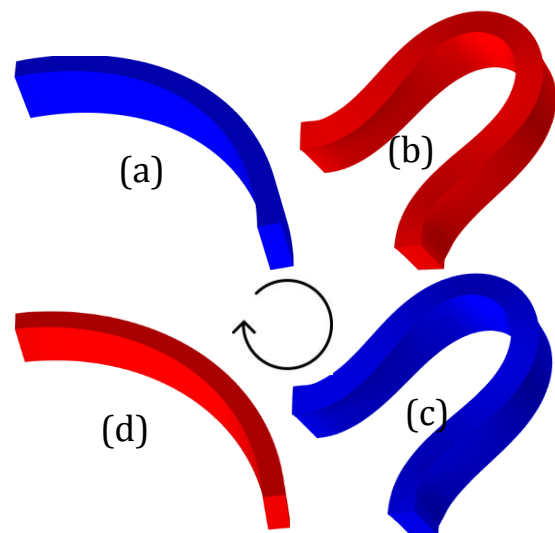


**Figure 1:** Shape memory cycle: (a) the original shape. (b) the deformed shape at 60°C. (c) the temporary shape obtained by cooling to 20°C. (d) the recovery shape obtained by heating up to 60°C.

**Acknowledgement:** Hauts-de-France Regional Council.

## 1. Introduction

Shape memory polymers (SMPs) are a class of smart materials that have the ability to recover their original shape from deformed and fixed shape called a temporary shape. The recovery phenomenon is triggered by an external stimulus [1] such as: temperature [2–4], the light exposure [5, 6], chemicals exposure [7]. The thermo-responsive shape memory polymers [2–4] have the ability to deform between two stable geometric configurations within a certain temperature range. The transition from one shape to another is caused by heating up to transition temperature. This temperature may refer to the glass transition temperature ( $T_g$ ) in the case of amorphous polymers such as Epoxy [8] or to melting temperature ( $T_m$ ) in the case of semi-crystalline polymers such as Poly (ethylene-co-vinyl acetate) (EVA, 25 wt% vinyl-acetate) [9].

Thermal-responsive SMPs can be classified into four different categories according to the nature of their permanent net points and the thermal transition related to the switching domains[10]:

- ✓ Chemically cross-linked thermoset amorphous polymers ( $T_r = T_g$ )
- ✓ Chemically cross-linked semi-crystalline polymer networks ( $T_r = T_m$ )
- ✓ Physically cross-linked amorphous copolymers ( $T_r = T_g$ )
- ✓ Physically cross-linked semi-crystalline block copolymers ( $T_r = T_m$ )

The semi-crystalline thermoplastic shape memory polyurethane (TPU-SMPU) is a physically cross-linked semi-crystalline block copolymer that has many advantages such as its ability to return to its original shape after many shape memory cycles in large strains (up to 400%). In addition, its recovery temperature is close to the human body which allows it to have a potential to be used in several biomedical applications since it has a good biocompatibility [11].

The TPU-SMPU is a physically cross-linked semi-crystalline polymer obtained by alternating two homopolymers constituting block copolymer. The first homopolymer (A) standing for the hard segment has higher melting temperature ( $T_{m_2} > 150^\circ\text{C}$ ) than the second (B) which stands for the soft segment. The melting temperature of the soft segment is the recovery temperature designated by  $T_r$  ( $T_r = T_{m_1}$ ). By heating the material above its  $T_{m_1}$  and below its  $T_{m_2}$ , only the soft segment is melted and the material behavior becomes rubber-like. Hard segment acts as crosslinks and they are responsible for the recovery of the original shape after being subjected to large deformation. If the polymer is cooled below  $T_{m_1}$ , the soft segment partially crystallizes and the material stiffens and loses its rubber-like behavior. If the material is cooled while it is deformed at the rubbery phase ( $T_{m_1} < T < T_{m_2}$ ), the soft segment crystallizes in the deformed configuration and newly forms other crystallites that act as temporary crosslinks which prevent the material from returning to its original shape. The recovery process is, then, triggered by reheating the material above its  $T_{m_1}$ . Figure 1 shows the corresponding state diagram.

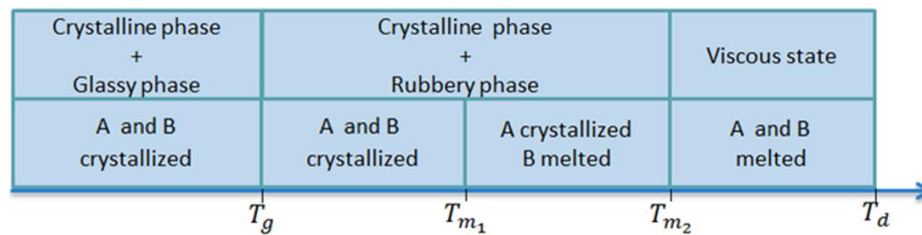


Figure 1. State diagram of thermoplastic semi-crystalline SMPU.

In this work, a 3D constitutive model based on finite viscoelastic phenomenological approach combined with the shape memory effect is proposed to describe the thermo-mechanical behavior of semi-crystalline shape memory polyurethane. In this model, the hyperelastic response is modeled by the generalized Mooney Rivlin model[12]. The viscoelastic over stress is given by internal variables solution of time-dependent evolution equations based on the generalized Maxwell rheological model. The material state is modeled by introducing an internal variable corresponding to the fraction of the crystallinity. The temperature-dependent evolution of the frozen fraction is introduced in finite viscoelastic model by applying an additional decomposition of the deformation gradient into elastic and stored parts [13].

## 2. Mechanical behavior testing

For mechanical and shape memory testing, SMPU granules, already vacuum dried at 80°C using a vacuum oven (Vacuum Oven XF120, Frances-Etuves) for 8 hours, were injection-molded (Thermo Scientific HAAKE MiniJet II) into standard specimen for tensile and shape memory tests. During injection molding, the temperature was kept at 190 °C and the mold temperature was kept at 20 °C. The injection molding holding pressure was 75 bars with a cooling time of 10 seconds.

The injection-molded specimens 5 mm wide, 1.52 mm thick and 50 mm long were subjected to classic shape memory cycles performed on tension machine (Instron model 1185, Instron France) equipped with a thermal chamber (Instron) to apply a specific temperature (for tensile and free recovery tests) or a specific heating ramps (for cooling and constrained length recovery) . Stresses were measured with a 1 kN load cell. The applied strain rate is set to 10 mm/min.

The typical thermo-mechanical recovery cycle consists of tensile deformation at 60°C ( $T_r + 18^\circ\text{C}$ ) and fixation the temporary shape by cooling to 20°C using liquid nitrogen. The applied strain (100%) stills stored due to the material lower molecular mobility below  $T_r$  . Then, free length or constrained length recovery are conducted when samples are subjected to a constant heating ramp ( $\dot{T} = 5^\circ\text{C}/\text{min}$ ). During the free length recovery, the uniaxial strain is recorded as the sample is stress-free, and during the constrained length recovery the stored strain is maintained and the stress is recorded as the sample is heated.

## 3. Experimental results

### 3.1. Tensile test at reference temperature

The uniaxial monotonic tensile tests were performed at 60°C in order to determine the most convenient hyperelastic model for the thermoplastic semi crystalline SMPU and cooled to

20°C to obtain the shape fixity. The experimental tensile curves were used in a curve fitting process to access mechanical properties.

Figure 3 depicts the tensile curves for 100% maximum strain for five successive cycles.

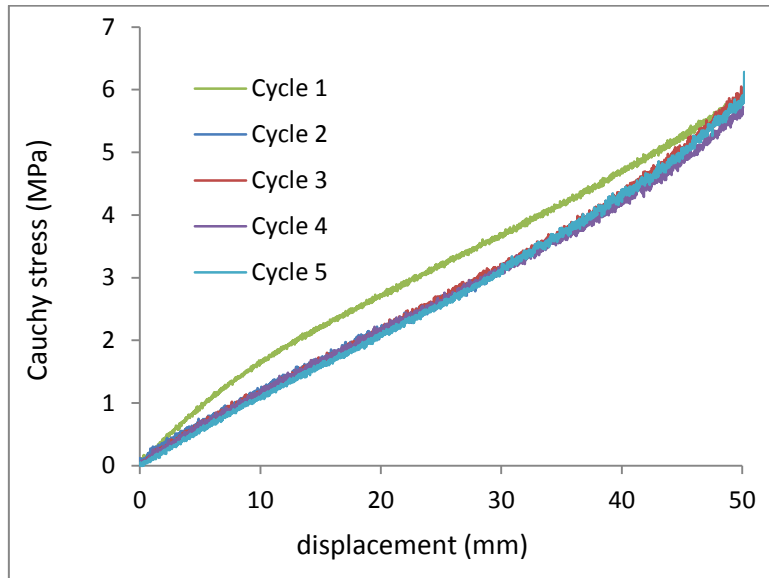


Figure 2. Stress–displacement diagram for 100% maximum strain:

As it is observed in figure 2, the tensile curve of the first cycle is slightly different from the four other curves which coincide. This due to the Mullins' effect [14].

### 3.2. Tensile-relaxation tests

During the tensile-relaxation tests, two different strain rates ( $10\text{mm}/\text{min}$  and  $5\text{mm}/\text{min}$ ) are applied on a cycled sample during 300s and 600s respectively to reach the same level of maximum strain (i.e:  $\varepsilon = 1$ :  $\Delta L = 50\text{mm}$ ). The stain holding period is set to 600s.

Figure 3 shows the corresponding Cauchy stress-displacement curves. These curves reveal the viscoelastic behavior of the material. Indeed, the evolution of the stress as a function of the strain is more important when the strain rate is higher.

Figure 4 shows the tensile-relaxation tests curves. During the relaxation process, the stress was observed during the same holding period and shows that the two curves converge to the same stress level.

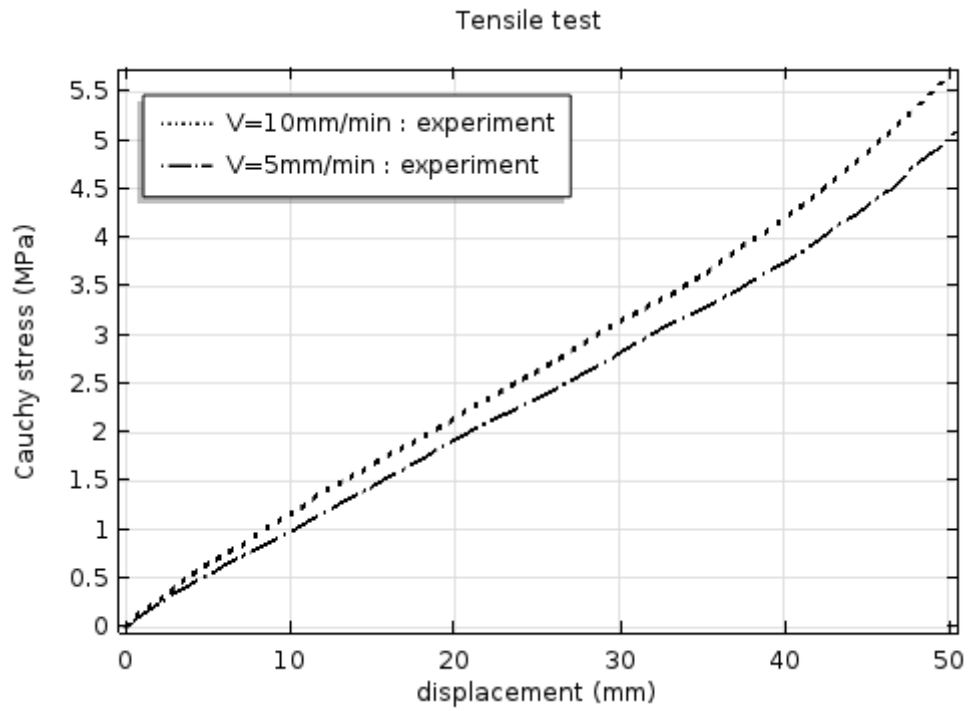


Figure 3. Tensile tests

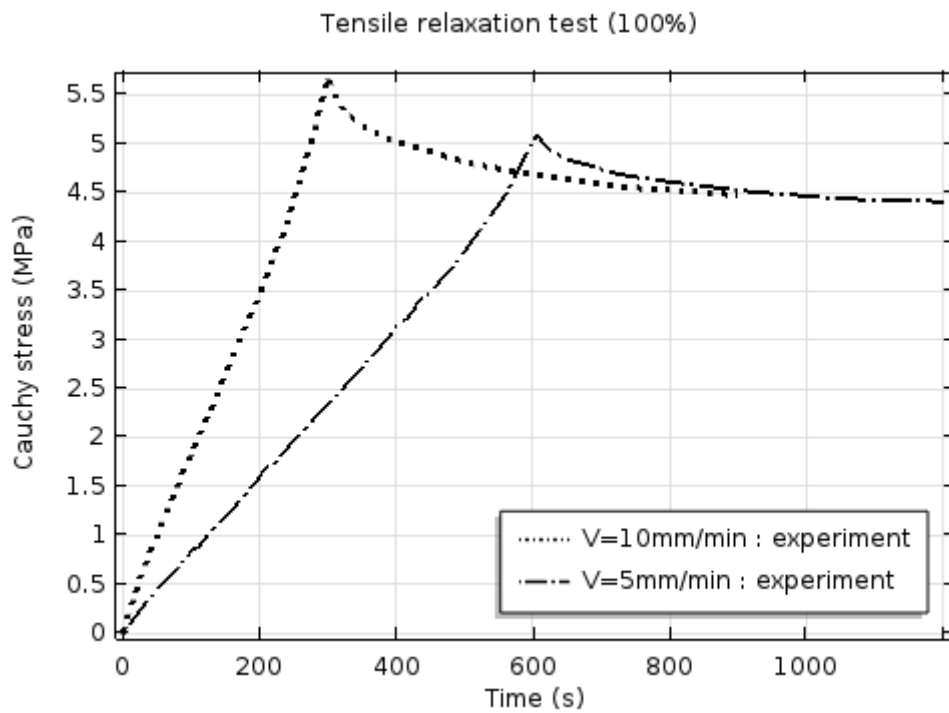


Figure 4. Tensile relaxation tests

### 3.3. *Unloading and cooling*

After unloading, the maximum strain, applied at the end of the tensile test, is approximately maintained. Shape fixity is obtained by cooling the sample after the tensile test (or after stress-relaxation test) below  $T_r$ . During cooling, the Cauchy stress decreases until reaching nearly zero. The shape fixity ratio is generally equal to 98% and the shape recovery ratio is generally equal to 100%.

### 3.4. *Fixed strain recovery*

Fixed strain recovery tests are performed by means of the tensile machine to measure the stress during heating. The heating rate was fixed to  $5^\circ\text{C}/\text{min}$ . Figure 5 shows the corresponding experimental results for two samples stretched to 100%.

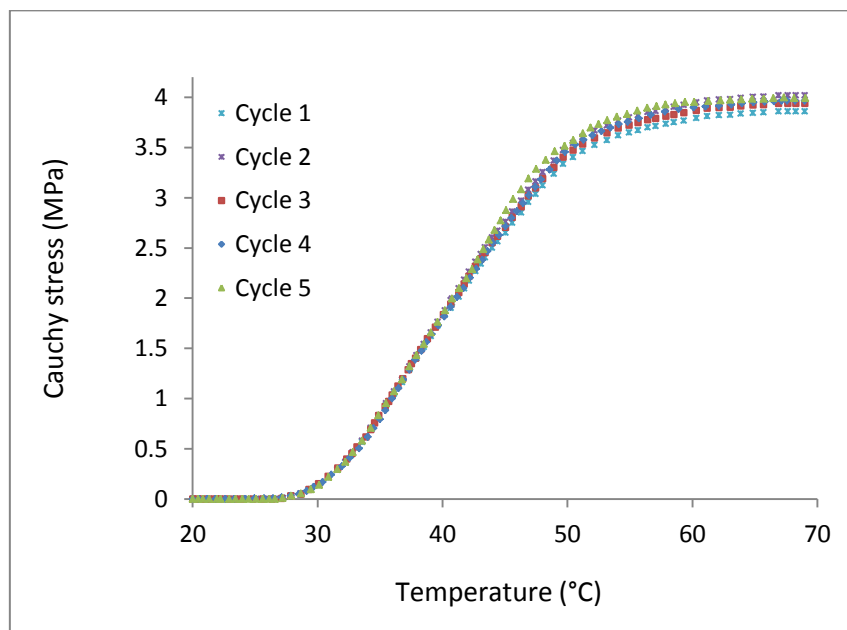


Figure 5. Fixed strain recovery.

## 4. Finite element modeling and simulation

### 4.1. *Modeling*

In order to describe the viscoelastic response and shape fixity and recovery of a shape memory polymer in large deformation, we introduce a 3D shape memory model based on two concepts. The first one is the definition of internal variables, through the multiplicative decomposition of the deformation gradient, in order to take into account the shape memory effect. The second is the finite linear viscoelasticity introduced by Simo [15] and Holzapfel [16].

The proposed model of SMPU is summarized in table 1.

Deformation	Stress response
$\underline{\underline{F}} = \underline{\underline{F}}_e \underline{\underline{F}}_s$	$\underline{\underline{S}} = g_\infty \underline{\underline{S}}_e + \sum_i^n \underline{\underline{Q}}_i$
$\underline{\underline{F}}_s = \underline{\underline{I}} + \phi_f \underline{\underline{H}}$	$\underline{\underline{S}}_e = \underline{\underline{S}}_e^{vol} + \underline{\underline{S}}_e^{iso}; \quad \underline{\underline{S}}_e^{vol} = Jp \underline{\underline{C}}_e^{-1}$
$\underline{\underline{C}}_e = \underline{\underline{F}}_s^{-T} \underline{\underline{C}} \underline{\underline{F}}_s^{-1}$	$\underline{\underline{S}}_e^{iso} = J^{-\frac{2}{3}} DEV \left( 2 \frac{\partial \Psi_e^{iso}}{\partial \underline{\underline{C}}} \right) = 2 \frac{\partial \Psi_e^{iso}}{\partial \underline{\underline{C}}}$
$\phi_f(T) = 1 - \frac{1-b}{1 + \exp(-a_1(T - T_r))} - \frac{b}{1 + \exp(-a_2(T - T_c))}$	$\Psi_e^{iso} = \sum_{i+j=1}^N c_{ij} (\bar{I}_{e1}-3)^i (\bar{I}_{e2}-3)^j$
	$\frac{d}{dt} \underline{\underline{Q}}_i + \frac{1}{\tau_i} \underline{\underline{Q}}_i = g_i \frac{d}{dt} \underline{\underline{S}}_e^{iso}$
	$\underline{\underline{Q}}_i = \int_0^t g_i \exp(-\frac{t-s}{\tau_i}) \frac{d}{ds} \underline{\underline{S}}_e^{iso} ds$
$\underline{\underline{\sigma}}(t) = \frac{1}{J} \underline{\underline{F}}(t) \underline{\underline{S}}(t) \underline{\underline{F}}^T(t) = \frac{1}{J} \underline{\underline{F}}(t) \left( g_\infty \underline{\underline{S}}_e + \int_0^t [g(t-s) - g_\infty] \frac{d}{ds} \underline{\underline{S}}_e^{iso} ds \right) \underline{\underline{F}}^T(t)$	

Table 1. The thermo-viscoelastic constitutive model for SMPU.

Where

- $\underline{\underline{F}}$  : The deformation gradient
- $\underline{\underline{F}}_s$  : The stored deformation gradient
- $\underline{\underline{F}}_e$  : The elastic deformation gradient
- $\phi_f$  : The frozen fraction function
- $\underline{\underline{I}}$  : The identity tensor
- $\underline{\underline{H}}$  : the displacement gradient tensor
- $\underline{\underline{C}}$  : The total right Cauchy-Green deformation tensor
- $\underline{\underline{C}}_e$  : The elastic part of  $\underline{\underline{C}}$
- $\underline{\underline{S}}$  : The second Piola-kirchoff stress
- $\underline{\underline{S}}_e^{iso}$  : the total isochoric response
- $\underline{\underline{Q}}_i$  : The viscoelastic overstress
- $\Psi_e^{iso}$  : The elastic deformation energy (Mooney Rivlin)
- $\underline{\underline{\sigma}}$  : The Cauchy stress

The parameters of the model are:

- $a_1, a_2$  et  $b$  : These parameters characterize the frozen fraction function identified from the experimental result of the free recovery test and using a fitting algorithm.
- $c_{ij}$ : These are the Mooney Rivlin constants: for 100% of strain, 4 parameters ( $c_{01}, c_{10}, c_{20}, c_{30}$ ) was sufficient to well predict the hyper elastic response.
- $g_i, \tau_i$ : These are the reduced relaxation coefficients and the corresponding relaxation times respectively.

The reduced relaxation function  $g(t)$  is defined by means of Prony series [17]:

$$\begin{cases} g(t) = g_\infty + \sum_{i=1}^n g_i \exp\left(-\frac{t}{\tau_i}\right) \\ g(0) = 1 \end{cases}$$

These parameters are determined by a curve fitting algorithm that minimizes the quadratic error between the experimental and theoretical results for the Cauchy stress:

$$\min_{p \in \Omega} \left( \sum_{i=1}^N [\sigma^{num}(t_i, p) - \sigma^{exp}(t_i)]^2 \right)$$

## 4.2. Simulation

### 4.2.1. Tensile-relaxation tests

For 100% of maximum applied strain, four hyperelastic parameters ( $C_{01}, C_{10}, C_{20}, C_{30}$ ) are assessed to describe the hyperelastic response. The experimental result for the tensile - relaxation tests for 100% of deformation is compared to numerical result. For the time dependent overstress calculation, four relaxation times are used to fit the viscous response. A very good agreement with the experiment has been found. The results are depicted in figure 6.

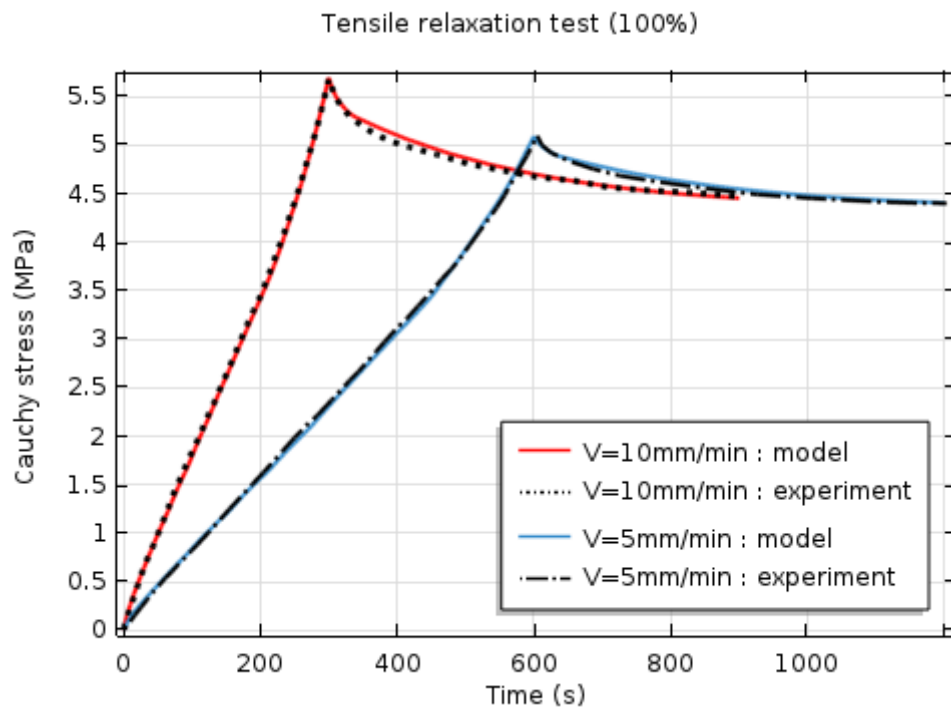


Figure 6. Tensile-relaxation tests: comparison between the model and the experiment.

#### 4.2.2. Shape memory cycle

Since the numerical results are similar for the five cycles, a comparison between the model and the experimental results are presented in this section only for the last cycle. Figure 7 depicts the shape memory cycle for 100% of deformation:

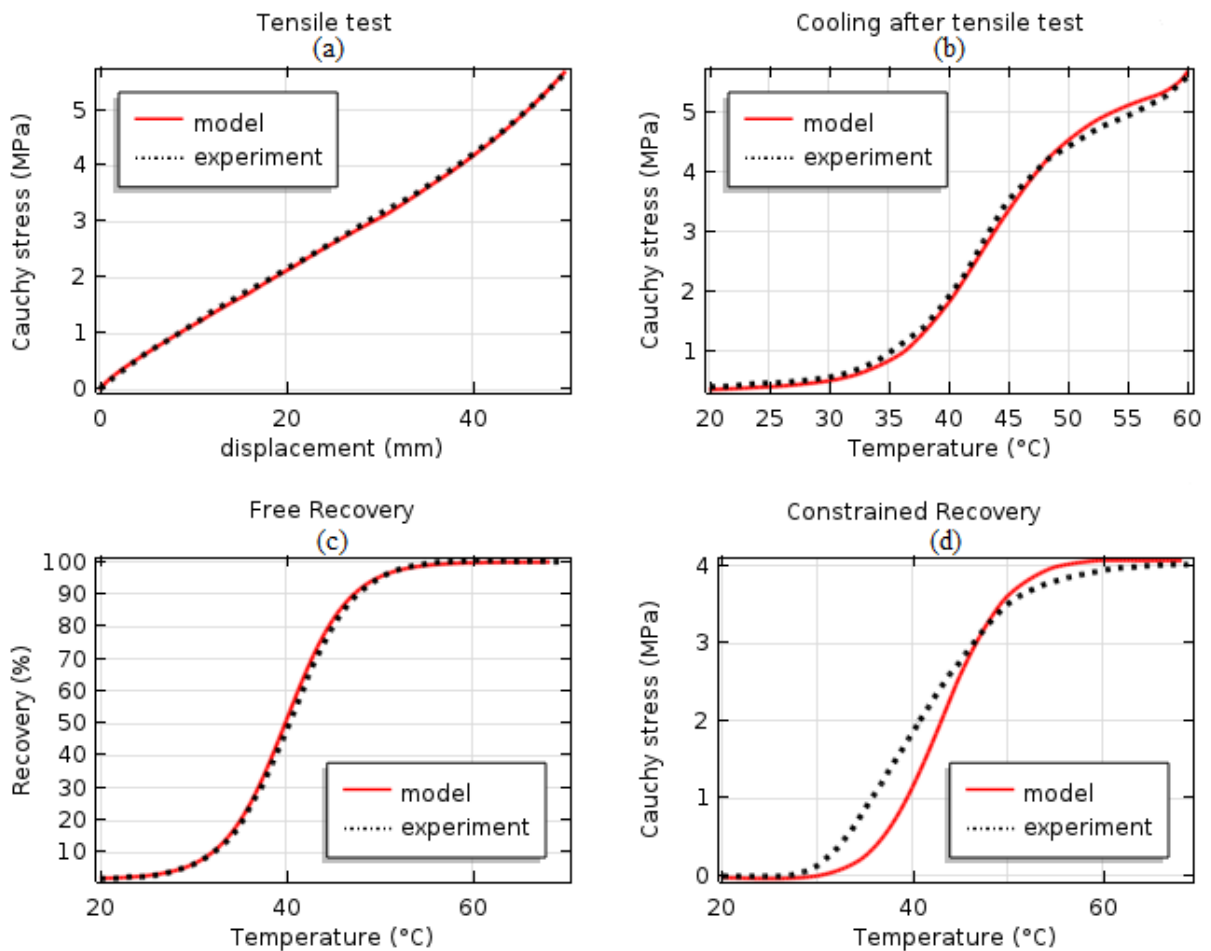


Figure 7. Shape memory cycle for a sample stretched to 100%: (a) Stress-displacement diagram, (b) Stress vs Temperature during cooling, (c) Free recovery and (d) Constrained recovery.

Figure 7.a shows the Cauchy stress – displacement diagram. Figure 7.b represents the evolution of the stress during cooling from 60°C to 20°C after the tensile test. We observe a decrease of the Cauchy stress from 60°C to 55°C due to the stress relaxation. From 55°C to 20°C, the stress continues to decrease due to a phase transition around the melting temperature (42°C) in addition to the stress relaxation, until reaching the minimum of the stress at 20°C. Figure 7.c represents the free recovery where the percentage of recovery is recorded during heating and figure 7.d represents the constrained recovery where the Cauchy stress is recorded during heating.

To assess the performance of our model, we propose to predict the shape memory response of 3D structure deformed in a 2D plane. A SMPU cylindrical ring with 23mm inner radius, 25mm outer radius and 2mm height has been tested for a shape memory cycle with multi-axial loading. A couple of two opposite prescribed displacements have been applied in two orthogonal directions as illustrated in figure 8. The sample has been subjected to a displacement equals to 15mm in each direction. Figure 9 shows the different shape (original shape, temporary shape and recovered shape) obtained experimentally.

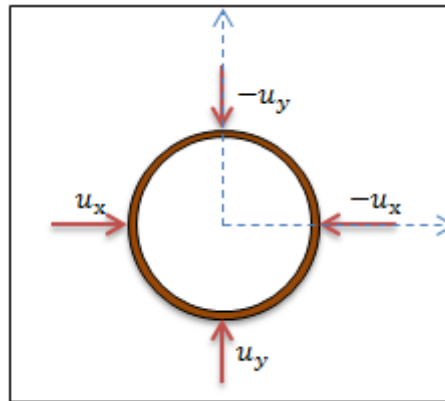


Figure 8. Illustration of the SMPU-Ring loading

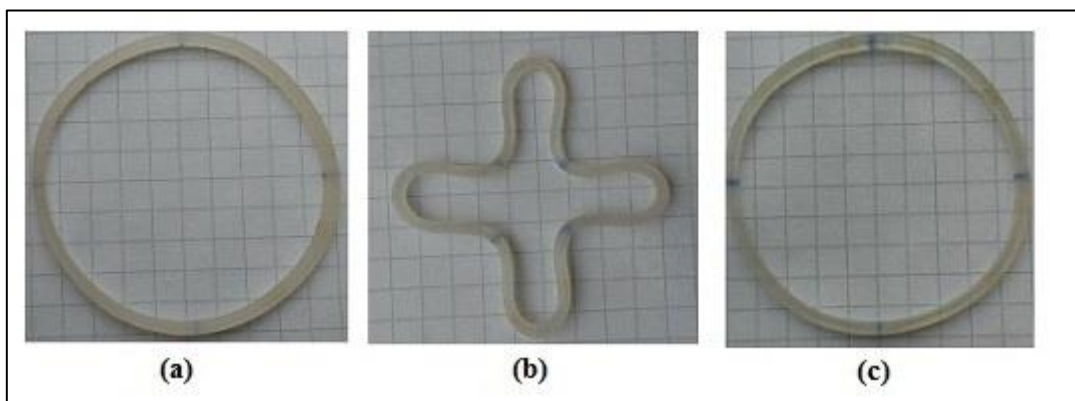


Figure 9. Experimental shape memory cycle applied on SMPU cylindrical ring: (a) the original shape. (b) the temporary shape. (c) the recovered shape.

For the numerical simulation, we assume that the distribution of the deformation within the sample is symmetric with respect to the centered horizontal and vertical axes. We consider, then, only the upper right quarter of the cylindrical ring. The applied displacement in horizontal and vertical directions is equal to  $15\text{mm}$  with a speed of  $10\text{mm}/\text{min}$ . Figure 10 shows the evolution of the shape during the free recovery test.

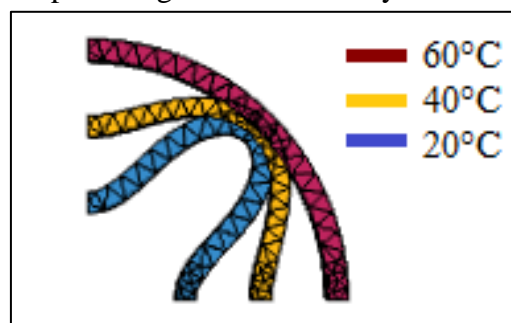


Figure 10. The evolution of the shape during the free recovery test

## 5. Conclusion

This paper presented thermo-visco-hyperelastic model for shape memory polymers under large strain. This model is based on two approaches. The first one is the finite viscoelasticity approach introduced by Simo [15] and Holzapfel [16] which extends the generalized Maxwell model to finite strain. This approach combines the viscoelastic response and the hyper-elastic response. The latter is determined from the Helmholtz free energy. In this model, we used the generalized Mooney Rivlin free energy. The second approach is the multiplicative decomposition of the deformation gradient used in Two-phase models in order to introduce the shape memory effect. This decomposition introduced the evolution of a frozen fraction function which controls the storage and release of the strain energy. The proposed thermo-visco-hyperelastic model has been tested for a shape memory cycle and gives a quantitative agreement with the experiment for shape memory cycle and relaxational behavior for two strain rates  $10\text{mm}/\text{min}$  and  $5\text{mm}/\text{min}$ . Furthermore, a cylindrical ring has been modeled for the shape memory cycle with multi-axial loads.

The proposed model has been implemented, for the first time, into Comsol Multiphysics to describe the thermo-mechanical cycle of a semi-crystalline shape memory polymer under large strain. This model is applicable for both amorphous and semi-crystalline shape memory polymers.

## References

- [1] Bouaziz R, Roger F, Prashantha K. Thermo-mechanical modeling of semi-crystalline thermoplastic shape memory polymer under large strain. *Smart Mater Struct* 2017; 26: 055009.
- [2] Liu Y, Gall K, Dunn ML, et al. Thermomechanics of shape memory polymer nanocomposites. *Mech Mater* 2004; 36: 929–940.
- [3] Small W, Singhal P, Wilson TS, et al. Biomedical applications of thermally activated shape memory polymers. *J Mater Chem* 2010; 20: 3356–3366.
- [4] Kazakevi R, Özarmut AÖ, Steeb H. Characterization of shape memory polymer estane by means of dynamic mechanical thermal analysis technique. *Smart Mater Res* 2014; 2014: 1–9.
- [5] Iqbal D, Samiullah MH. Photo-responsive shape-memory and shape-changing liquid-crystal polymer networks. *Materials (Basel)* 2013; 6: 116–142.
- [6] Li MH, Keller P, Li B, et al. Light-driven side-on nematic elastomer actuators. *Adv Mater* 2003; 15: 569–572.
- [7] Huang WM, Zhao Y, Zhang JL, et al. Chemo-responsive Shape Memory/change Effect in Polymeric Materials Based on Transport Phenomena. *J Fluid Flow, Heat Mass Transf* 2014; 1: 16–22.

- [8] Arrieta JS, Diani J, Gilormini P. Cyclic and monotonic testing of free and constrained recovery properties of a chemically crosslinked acrylate. *J Appl Polym Sci* 2014; 131: 1–8.
- [9] Li J, Rodgers WR, Xie T. Semi-crystalline two-way shape memory elastomer. *Polymer (Guildf)* 2011; 52: 5320–5325.
- [10] Liu C, Qin H, Mather PT. Review of progress in shape-memory polymers. *J Mater Chem* 2007; 17: 1543.
- [11] Cabanlit M, Maitland D, Wilson T, et al. Polyurethane shape-memory polymers demonstrate functional biocompatibility in vitro. *Macromol Biosci* 2007; 7: 48–55.
- [12] Rivlin RS, Saunders DW. Large elastic deformations of isotropic materials VII. Experiments on the deformation of rubber. *Springer Sci Media* 1951; 243: 251–288.
- [13] Sadik S, Yavari A. On the origins of the idea of the multiplicative decomposition of the deformation gradient. *Math Mech Solids* 2015; 2–4.
- [14] Diani J, Fayolle B, Gilormini P. A review on the Mullins effect. *Eur Polym J* 2009; 45: 601–612.
- [15] Simo JC. On a fully three dimensional finite strain viscoelastic damage model : Formulation and computational aspects. *Comput Methods Appl Mech Eng* 1987; 60: 53–173.
- [16] Holzapfel G. On large strain viscoelasticity : continuum formulation and finite element applications to elastomeric structures. *Int J Numer Methods Eng* 1996; 39: 3903–3926.
- [17] Fung YC. *Biomechanics*. New York, NY: Springer New York, 1981. Epub ahead of print 1981. DOI: 10.1007/978-1-4757-1752-5.

# Synthesis and Characterization of a Mn-based Metal-organic framework

Wararat TRANGANPHAIBUL<sup>1\*</sup>, Sareeya BUREEKAEW<sup>1</sup>

<sup>1</sup>School of Energy Science and Engineering, Vidyasirimedhi Institute of Science and Technology (VISTEC), 555 Moo 1 Payupnai, Wangchan, Rayong 21210, Thailand

## Abstract

A three-dimensional cationic Mn-based metal-organic framework with empirical formula of  $[[\text{Mn}_4(\text{bdc-NH}_2)_{1.5}(\text{HCOO})_3]^{2+}]_n$  (**1**) ( $\text{NH}_2\text{-bdc}$  = 2-Amino-1,4-benzenedicarboxylic acid) has been synthesized by solvothermal synthesis method under mild condition. It was characterized by single crystal X-ray diffraction, powder X-ray diffraction and TGA. Crystallographic data reveal that this compound possesses one dimensional channel with the diameter of  $\sim 8$  Å.

## Introduction

Metal-organic frameworks (MOFs) also known as porous coordination polymers (PCPs) are a class of porous materials consisting of both inorganic metal ions/clusters and organic ligands<sup>1</sup>. Due to their crystallinity, high porosity and surface area, and their large structural variety, MOFs provide a vast range of potential applications in e.g., gas storage<sup>2-4</sup>, catalyst<sup>5-6</sup>, and separation<sup>7</sup>. Herein, we present a study of 3D a MOF,  $[\text{Mn}_4(\text{NH}_2\text{-bdc})_{1.5}(\text{HCOO})_3]^{2+}$  (**1**) ( $\text{NH}_2\text{-bdc}$  = 2-Amino-1, 4-benzenedicarboxylic acid) with 1D channels.

## Synthesis of $[\text{Mn}_4(\text{bdc-NH}_2)_{1.5}(\text{HCOO})_3](\text{NO}_3)_2$ (**1**)

All chemicals for synthesis were commercially available reagents of analytical grade and were used without further purification. For single crystal of **1**,  $\text{Mn}(\text{NO}_3)_2 \cdot 4\text{H}_2\text{O}$  0.4 mmol and  $\text{NH}_2\text{-bdc}$  0.4 mmol were dissolved in mixed DMF (2.5 ml), and deionized water (2.5 ml). Next, the mixture was heated to 100°C for 1 day and then the temperature was increased to 120°C for 12 hr. After finished the reaction, deep brown crystals were obtained.

## Crystal structure of $[\text{Mn}_4(\text{NH}_2\text{-bdc})_{1.5}(\text{HCOO})_3](\text{NO}_3)_2$ (**1**)

X-ray crystallography revealed that complex **1** crystallizes in the orthorhombic,  $C2/c$  space group, and the asymmetric unit contains four crystallographically independent Mn(II) ions, one and half  $\text{NH}_2\text{-bdc}$  ligands, and three formate as depicted in Figure 1a. Mn(II) ions are in slightly distorted octahedral environment coordinated by six oxygen atoms from six carboxylate groups (three  $\text{NH}_2\text{-bdc}$  and three formate). Complex **1** consists of macrocycles built up with twelve Mn atoms held together by carboxylate groups from  $\text{NH}_2\text{-bdc}$  and formate. Each ring connects with six adjacent ones forming Mn-carboxylate 2D sheets which are linked each other by  $\text{NH}_2\text{-bdc}$  ligands. The resulting cationic framework exhibits 1D channels along  $c$ -axis (Figure 1b – and 1c) with the diameter of  $\sim 8$  Å. Figure 1e reveals XRD pattern between as-synthesized and simulated. Note that no direct evidence of the charge-balancing anions was obtained from crystallographic data. Since  $\text{Mn}(\text{NO}_3)_2 \cdot 4\text{H}_2\text{O}$  was used in the synthesis, nitrate ( $\text{NO}_3^-$ ) is expected to neutralize the framework. IR spectroscopy of as-synthesized framework (shown in Figure 2) shows the characteristic peak of N-O at  $1,380\text{ cm}^{-1}$ , indicating the existence of  $\text{NO}_3^-$  in the framework.

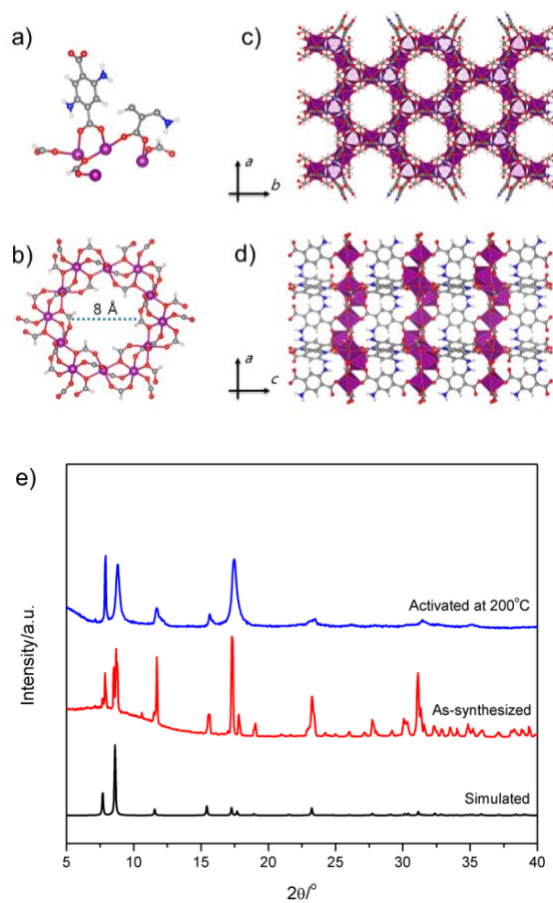


**Figure 1.** a) Asymmetric unit of **1**, b) Mn(II)-carboxylate macrocycle with pore dimension of  $\sim 8$  Å, b) 2D plane connected Mn-macrocycles viewing along *c*-axis in **1**, c) view of Mn-macrocycle planes bridged by NH<sub>2</sub>-bdc ligands and e) Simulated patterns from X-ray structure, powder X-ray diffraction patterns for as-synthesized and activated of **1**.

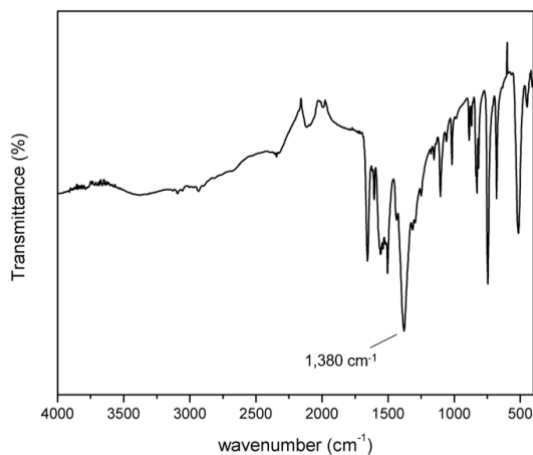


Figure 2. FTIR spectra of as-synthesized **1**

### Thermal Analysis

Thermogravimetric analysis profile of the as-synthesized complex **1** displays four main steps of weight loss as depicted in Figure 3. The first and second steps indicated weight loss of ~15% in the temperature range of 20–200°C can be attributed to the loss of guest molecules, such as adsorbed water and DMF. The third and fourth step in the temperature range of 250 – 400°C is due to the decomposition of organic linkers, indicating that the framework is stable up to 250°C. Measurement condition is under nitrogen gas, 100 ml/min flow rate and 10°C/min temperature rate.

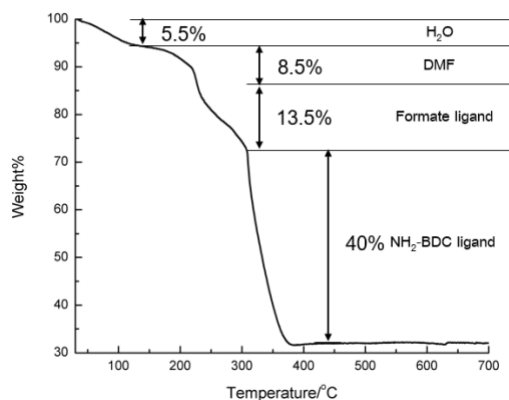
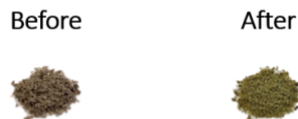


Figure 3. TG curve of as-synthesized **1** in the temperature range of room temperature to 700°C.

According to the TGA data, solvent molecules should be removed at 200°C. Complex **1** was activated by heating at 200°C under vacuum for 6 h. The color of the sample change from deep brown to yellow after the activation (Figure 4) but still maintaining the structure as evidenced by the XRPD



**Figure 4.** Color of **1** before and after heating at 200°C under vacuum to remove all solvent molecules.

patterns. The peak positions of as-synthesized and activated samples are similar with different intensity. This color change possibly originates from the changing of oxidation state of Mn ions in the frameworks. (show in Figure 1e)

### Conclusions

In summary, we have successfully synthesized a new manganese-based metal-organic frameworks,  $[\text{Mn}_4(\text{formate})_3(\text{BDC-NH}_2)_{1.5}]$  (**1**) with  $\text{NO}_3^-$  as anionic counterion. The Mn-MOF provides one dimensional channel with the diameter of  $\sim 8 \text{ \AA}$ . It was found that after the activation to remove all solvent molecules from the channel, the color of this MOF changes from dark brown to yellow possibly indicative of changing the oxidation state of Mn ion.

### References

1. Kitagawa, S.; Kitaura, R.; Noro, S., Functional porous coordination polymers. *Angew. Chem. Int. Ed. Engl.*, **2004**, *43* (18), 2334-75.
2. Ma, S.; Zhou, H. C., Gas storage in porous metal-organic frameworks for clean energy applications. *Chem Commun*, **2010**, *46* (1), 44-53.
3. Mishra, P.; Edubilli, S.; Mandal, B.; Gumma, S., Adsorption of  $\text{CO}_2$ ,  $\text{CO}$ ,  $\text{CH}_4$  and  $\text{N}_2$  on DABCO based metal organic frameworks. *Microporous and Mesoporous Materials* **2013**, *169*, 75-80.
4. Rosi, N. L.; Eckert, J.; Eddaoudi, M.; Vodak, D. T.; Kim, J.; Keeffe, M.; Yaghi, O. M., Hydrogen Storage in Microporous Metal-Organic Frameworks. *Science* **2003**, *300* (5622), 1127.
5. Thallapally, P. K.; Fernandez, C. A.; Motkuri, R. K.; Nune, S. K.; Liu, J.; Peden, C. H. F., Micro and mesoporous metal-organic frameworks for catalysis applications. *Dalton Transactions* **2010**, *39* (7), 1692-1694.
6. Cundy, C. S.; Cox, P. A., The Hydrothermal Synthesis of Zeolites: History and Development from the Earliest Days to the Present Time. *Chemical Reviews* **2003**, *103* (3), 663-702.
7. Li, J.-R.; Kuppler, R. J.; Zhou, H.-C., Selective gas adsorption and separation in metal-organic frameworks. *Chemical Society Reviews* **2009**, *38* (5), 1477-1504.

# Crystal Engineering of Bimetallic Metal-Organic Frameworks based on MIL-101

T. Tanasaro,<sup>1\*</sup> S. Bureekaew,<sup>1</sup>

<sup>1</sup> School of Energy Science and Engineering, Vidyasirimedhi Institute of Science and Technology (VISTEC), 555 Moo 1 Payupnai, Wangchan, Rayong 21210, Thailand.

## Abstract

Based on by mixed-metal approach, bimetallic MIL-101(Cr, Fe) was successfully synthesized through an environmental friendly hydrofluoric acid-free solvothermal method. The effects of the second metal (Fe) on the morphology of the nanocrystal and on adsorption property of the mixed-metal MIL-101(Cr, Fe) were examined. The obtained materials were characterized by using Powder X-ray Diffraction (PXRD), Scanning electron microscope (SEM), Energy-dispersive X-ray spectroscopy (EDS) and N<sub>2</sub> adsorption.

## 1. Introduction

Metal-organic frameworks (MOFs), a class of crystalline porous hybrid materials are composed of metal ions or metal clusters linking with organic ligands to form a framework. Due to their characteristics such as high surface area, high pore volume and tunable pore size MOFs are attractive in many applications involving drug delivery,<sup>1</sup> gas adsorption/separation,<sup>2-7</sup> and catalysis.<sup>8</sup> However, MOFs still have some limitations on chemical and thermal durability and moderate catalytic activity when compared to other porous materials (zeolite<sup>9</sup> or carbon-based materials).<sup>10</sup> Therefore, to overcome such limitations, MOFs have been developed continuously by several methods. Ligand design and post-synthetic modification on the linkers are well-known methods to create the active sites for catalytic and adsorption applications. Note that, the bulky functionalized moieties sometimes block the access of guest molecules to the framework.<sup>11</sup> Guest encapsulation is another strategy to introduce the catalytic activity into MOFs. The inert framework will be active when catalytically active guest molecules such as metals nanoparticles (NPs) is incorporated.<sup>12</sup> However, this approach is often limited by the size of pore windows. Large guest molecules cannot access into the pore whereas small guest molecules possibly leach out from the framework. Recently, mixed metal approach has been employed to prepare solid-solution-like MOFs. The incorporation of two or three different metals in the same framework allows the mixed-metal MOFs exhibiting new functions or showing the properties superior to their parent MOFs. Some studies have shown that the mixed-metal MOFs exhibit gas adsorption capacity higher than their parent MOFs<sup>13,14</sup> and some provide excellent catalytic activity which is not found in the parent compounds.<sup>15</sup> MIL-101(Cr), one type of MOFs, resembles the augmented MTN zeolite topology, consisting of two type of inner cages with diameters of 2.9 and 3.4 nm accessible through windows of ca 1.2 and 1.6 nm. MIL-101(Cr) presents extremely large surface area (BET surface area of 4100 m<sup>2</sup>/g and cell volume of ~702,000 Å<sup>3</sup>), high concentration of coordinately free Cr ions, and a remarkable stability towards air, water, common solvents and thermal treatment (up to 300°C).<sup>16</sup> These attributes make MIL-101(Cr) suitable for several applications. In this work, we aim to achieve new mixed-metal MOFs of MIL-101(Cr) and study the effect of the second metal on their properties such as morphology and adsorption.

## 2. Experimental

### Preparation of MIL-101(Cr)

MIL-101(Cr) was synthesized according to the literature with some modifications.<sup>17</sup> Typically, 2 g (5 mmol) of Cr(NO<sub>3</sub>)<sub>3</sub>·9H<sub>2</sub>O was dissolved in 24 mL of deionized water and 0.83 g (5 mmol) of terephthalic acid was added. The mixture was charged in to the 50 mL Teflon line autoclave and heated in the oven at 220°C for 8 h. The reaction was cooled to room temperature for 12 h. The green solid powder was collected and stirred in DMF two times at 80 °C for 30 min each. Then the sample was

stirred with hot ethanol at 80 °C for 24 h to let ethanol replace the DMF accommodated in the framework. Finally, the solid was dried at 80 °C for overnight.

### Preparation of MIL-101(Cr, Fe)

MIL-101(Cr, Fe) was synthesized using a method identical with MIL-101(Cr). Typically,  $\text{Cr}(\text{NO}_3)_3 \cdot 9\text{H}_2\text{O}$  and  $\text{FeCl}_3 \cdot 6\text{H}_2\text{O}$  were dissolved in 24 mL of deionized water. Then 0.83 g (5 mmol) of terephthalic acid was added. The mixture was charged in to the 50 mL Teflon lined autoclave and followed the same step as MIL-101(Cr). The ratio of  $\text{Cr}(\text{NO}_3)_3 \cdot 9\text{H}_2\text{O}$  and  $\text{FeCl}_3 \cdot 6\text{H}_2\text{O}$  added as the reactants in each synthesis were 4.75:0.25, 4.5:0.5, 4.25:0.75, 3.75:1.25 and 3.33:1.67 mmol resulting **1**, **2**, **3**, **4** and **5** respectively.

## 3. Results and discussion

### Powder X-ray Diffraction (PXRD)

The powder X-ray diffraction patterns of MIL-101(Cr), **1** and **2**, resemble the simulated pattern of MIL-101(Cr) indicating that they are isostructural. **3** and **4** showed additional peaks at  $2\theta \approx 10 - 11$  attributed to the existence of a mixed-phase structure consisting of dominant MIL-101. Furthermore, **5** exhibits PXRD pattern different from that of MIL-101(Cr) but similar to that of the minor phase in **3** and **4** as shown in Figure 1. As confirmed from the distinct PXRD patterns, mixed metal MIL-101(Cr) cannot be formed at 1.67 mmol of sample **5**.

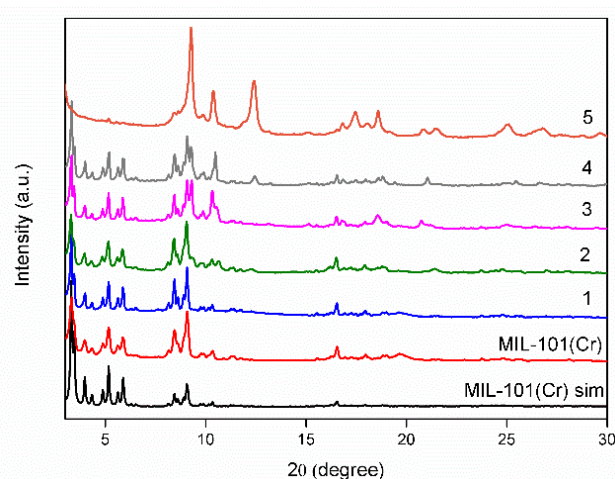


**Figure 1** Powder X-ray diffraction patterns of MIL-101(Cr) and MIL-101(Cr, Fe).

### Scanning Electron Microscopy (SEM)

MIL-101(Cr) has uniform spherical morphology characterized using SEM as shown in Figure 2a. The particle size is approximately 100 nm. Differed from parent MIL-101(Cr), **1** and **2** shows pure phase octahedral morphology as depicted in Figure 2a and b. The particle size of **1** significantly increases into 300 - 400 nm. For **2**, the particle size increases into 400 - 700 nm but not monodispersed. Moreover, some part of **3**, **4** exhibits octahedral particle but mixed with other phases as seen in Figure 3c and d. These results agree with the PXRD that **3** and **4** are formed in mixed phase. Figure 3f shows morphology of **5** with irregular shape without any trace of octahedral MIL-101 as revealed in PXRD. SEM results indicate that the incorporation of Fe into MIL-101(Cr) has the impact on the morphology of MIL-101(Cr).

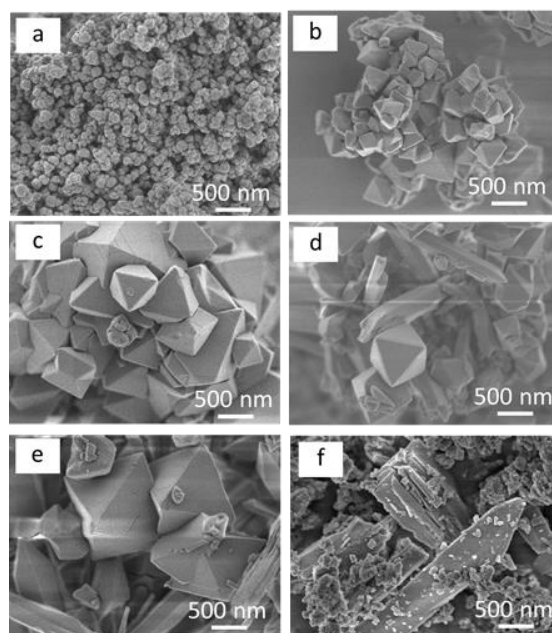


**Figure 2** SEM images of (a) MIL-101(Cr), (b) **1**, (c) **2**, (d) **3**, (e) **4**, and (f) **5**.

### Gas adsorption

N<sub>2</sub> adsorption isotherm was measured at 77K after activated at 150°C for 10 h. All materials show large void volume. The shape of resulting isotherms (Figure 3) shows the characteristic of material with a combination of micro- and mesopores as expected for the typical MIL-101.<sup>16</sup> BET surface area of all systems are summarized in Table 1. For **2**, provides highest surface area when compare to parent MIL-101(Cr). However, the surface area dramatically decreases when the amount of Fe is larger than 0.75 mmol which presents the unknown phase in the sample **3**, **4**, and **5**.

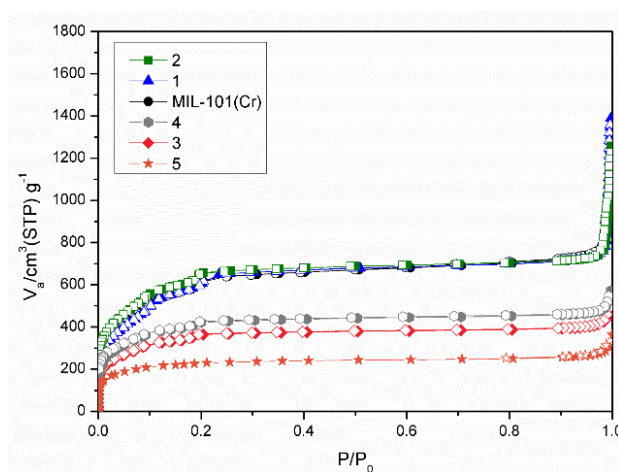


**Figure 3** N<sub>2</sub> adsorption isotherm at 77K after activated at 150°C for 10 h.

**Table 1.** BET surface area and total pore volume of MIL-101(Cr) and MIL-101(Cr, Fe) from N<sub>2</sub> isotherm

	MIL-101(Cr)	<b>1</b>	<b>2</b>	<b>3</b>	<b>4</b>	<b>5</b>
S <sub>BET</sub> (m <sup>2</sup> g <sup>-1</sup> )	2127	2273	2317	1280	1485	832

### Energy-dispersive X-ray spectroscopy (EDS)

The distribution of metal in **2** which exhibits pure phase octahedral morphology and highest surface area was determined by EDS. The result shows a good distribution of Fe in mixed-metal MIL-101(Cr) as shown in Figure 4.

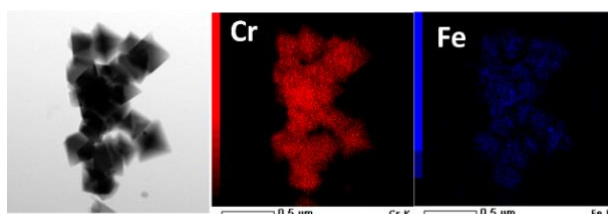


**Figure 4** TEM image and the corresponding EDS element mapping of the **2**, Cr (red) and Fe (blue).

### 4. Conclusion

In this work, the incorporation of Fe<sup>3+</sup> into MIL-101(Cr) was successful. The incorporation of Fe<sup>3+</sup> leads to increase in the particle size and improved morphology of MIL-101(Cr).

### References

1. A. Corma, H. Garc'ia and F. X. Llabr'es i Xamena, *Chem. Rev.*, 2010, **110**, 4606.
2. A. R. Millward and O. M. Yaghi, *J. Am. Chem. Soc.*, 2005, **127**, 17998.
3. A. O. Yazaydin, R. Q. Snurr, T. H. Park, K. Koh, J. Liu, M. D. LeVan, A. I. Benin, P. Jakubczak, M. Lanuza, D. B. Galloway, J. J. Low and R. R. Willis, *J. Am. Chem. Soc.*, 2009, **131**, 18198.
4. J. R. Li, R. J. Kuppler and H. C. Zhou, *Chem. Soc. Rev.*, 2009, **38**, 1477.
5. J. Kim, S. T. Yang, S. B. Choi, J. Sim, J. Kim and W. S. Ahn, *J. Mater. Chem.*, 2011, **21**, 3070.
6. D. A. Yang, H. Y. Cho, J. Kim, S. T. Yang and W. S. Ahn, *Energy Environ. Sci.*, 2012, **5**, 6465.
7. J. R. Li, Y. Ma, M. C. McCarthy, J. Sculley, J. Yu, H. K. Jeong, P. B. Balbuena and H. C. Zhou, *Coord. Chem. Rev.*, 2011, **255**, 1791.
8. P. Horcajada, T. Chalati, C. Serre, B. Gillet, C. Sebrie, T. Baati, J. F. Eubank, D. Heurtaux, P. Clayette, C. Kreuz, J. S. Chang, Y. K. Hwang, V. Marsaud, P. N. Bories, L. Cynober, S. Gil, G. F'erey, P. Couvreur and R. Gref, *Nat. Mater.*, 2010, **9**, 172.
9. B. M. Weckhuysen and J. Yu, *Chem Soc Rev*, 2015, **44**, 7022.
10. L. L. Zhang and X. S. Zhao, *Chem Soc Rev*, 2009, **38**, 2520.
11. M. Lin Foo, S. Horike, T. Fukushima, Y. Hijikata, Y. Kubota, M. Takata and S. Kitagawa, *Dalton Trans*, 2012, **41**, 13791.
12. B. Li, Y. Zhang, D. Ma, T. Ma, Z. Shi and S. Ma, *J Am Chem Soc*, 2014, **136**, 1202.
13. Z. Zhou, L. Mei, C. Ma, F. Xu, J. Xiao, Q. Xia and Z. Li, *Chemical Engineering Science*, 2016, **147**, 109.
14. C. H. Lau, R. Babarao and M. R. Hill, *Chem Commun (Camb)*, 2013, **49**, 3634.
15. D. Sun, F. Sun, X. Deng and Z. Li, *Inorg Chem*, 2015, **54**, 8639.
16. G. Ferey, C. M. Draznieks, C. Serre, F. Millange, J. Dutour, S. Surble, I. Margiolaki, *Science.*, 2005, **309**, 2040.
17. Z. Liang, M. Marshall, C. H. Ng and A. L. Chaffee, *Energy & Fuels*, 2013, **27**, 7612.

# Comparison between flexible PZT and BTO piezoelectric films for mechanical energy harvesting

Seveno Raynald, Dufay Thibault and Guiffard Benoit  
Université Bretagne Loire, Université de Nantes, IETR UMR CNRS 6164, France

## Abstract

Due to the recent development of flexible perovskite-based thin films, the interest for this kind of material has increased, especially in the field of piezoelectricity and energy harvesting at low frequency. In order to anticipate some industrial developments, the fabrication process of these films has to be as simple as possible. In this aim, flexible lead zirconate titanate (PZT) films have been realized by a chemical solution deposition process (CSD) where no vacuum technique is needed. These films exhibit good ferroelectric and piezoelectric properties, which allow competing with polymeric piezoelectric films, such as polyvinylidene fluoride (PVDF) films, in flexible applications. However, the wide use of PZT films is limited by applications which require lead-free materials. In order to enlarge the panel of the flexible perovskite-based thin films, Barium titanate (BTO) films have been realized with a similar CSD process by using a metallic foil as substrate. Dielectric, ferroelectric and piezoelectric properties of both PZT and BTO films have been compared, as a function of process parameters. In a next step, these films have been encapsulated in a polyethylene terephthalate (PET) film in order to obtain a flexible piezoelectric generator. The energy densities harvested by PZT and BTO films have been measured under mechanical stress at 1Hz.

**Keywords:** PZT, BTO, piezoelectricity, flexibility, thin films

## 1. Introduction

Energy harvesting devices are widely studied to offer some solutions to the energy crises, trying to use a maximum of environmental and renewable natural energy sources, such as classical solar cells [1] and electromagnetic [2] or electrostatic [3] generators. Piezoelectric materials are of great interest because they are able to convert the mechanical energy into electricity, which offers many possibilities of energy harvesting devices. Generally, piezoelectric generators are activated in a vibrational mode, by using massive ceramics, or thin films deposited onto stiff substrates like silicon, sapphire or alumina. To harvest air flow's energy, flexible piezoelectric thin film can be used as synthetic blade of grass, which will be able to produce electricity by its large deformation under the air flow.

In this paper, the preparation and the characterizations of flexible piezoelectric thin films of lead zirconate titanate (PZT) and barium titanate (BTO) will be described and the corresponding harvested power under alternative mechanical strain at 1 Hz will be compared.

## 2. Thin film preparation

To be crystallized, PZT and BTO thin films should be heat-treated at temperatures more than 600 °C and 700 °C respectively, avoiding the common used flexible polymeric substrates such as polyimide films (Kapton) which can support a maximum temperature of about 450 °C. One alternative route is the use of a thin metallic foil as substrate. Indeed, metals can generally support high temperatures and could be flexible if the thickness is sufficiently thin. In table 1 are reported the interesting properties of several metallic foils which could be used as potential substrates. In the goal of airflow's harvesting applications, metallic foil should exhibit Young's modulus and density as low as possible. Fusion temperature should be higher than the crystallization temperature of piezoelectric films and thermal expansion coefficient should be higher than these of piezoelectric films (about  $5 \times 10^{-6} \text{ }^\circ\text{C}^{-1}$  [4]) in order to limit cracks during the heat-treatment. Aluminium foil appears to be a good candidate, especially because it is very lightweight and has a Young's modulus (69 GPa) inferior to that of PZT (96 GPa). However, its low melting temperature (660 °C) does not allow its use as substrate in

the case of BTO films, where a nickel foil will be preferred. As a comparison, PZT films will be deposited onto aluminium and nickel foils.

Table 1. Comparison between different metallic substrates properties.

Metal	Fusion T° (°C)	Young's Modulus (GPa)	Thermal expansion coefficient ( $\times 10^{-6} \text{ } ^\circ\text{C}^{-1}$ )	Density ( $\text{g/cm}^3$ )
Platinum	1772	276	9	21.5
Copper	1083	124	17	9
Stainless steel	1400	200	18	7.9
Nickel	1453	177	13	8.3
Aluminium	660	69	23	2.7
Tungsten	3410	411	4.5	19.3
Molybdenum	2617	329	5	10.2

In order to easily transfer the fabrication process to the industry for mass production, piezoelectric films have been obtained by a Chemical Solution Deposition process (CSD) where no vacuum technique is used, based on alkoxide precursors [5], [6]. Lead and barium acetates are dissolved in acetic acid, zirconate and titanate n-propoxides are mixed to obtain a Zr/Ti ratio of 57/43 (in the case of PZT films). Ethylene glycol is then added to limit the cracks during the firing process [7]. The final precursor solutions are spin-coated onto aluminium (16  $\mu\text{m}$  thick) and nickel (20  $\mu\text{m}$  thick) foils at 6000 rpm and the firing process (650  $^\circ\text{C}$  for 2 minutes and 750  $^\circ\text{C}$  for 15 minutes for PZT and BTO films, respectively) allows the crystallization of the piezoelectric films. By multiple coating, final PZT and BTO films of 3  $\mu\text{m}$  and 4.5  $\mu\text{m}$  in thickness have been obtained respectively (figure 1).

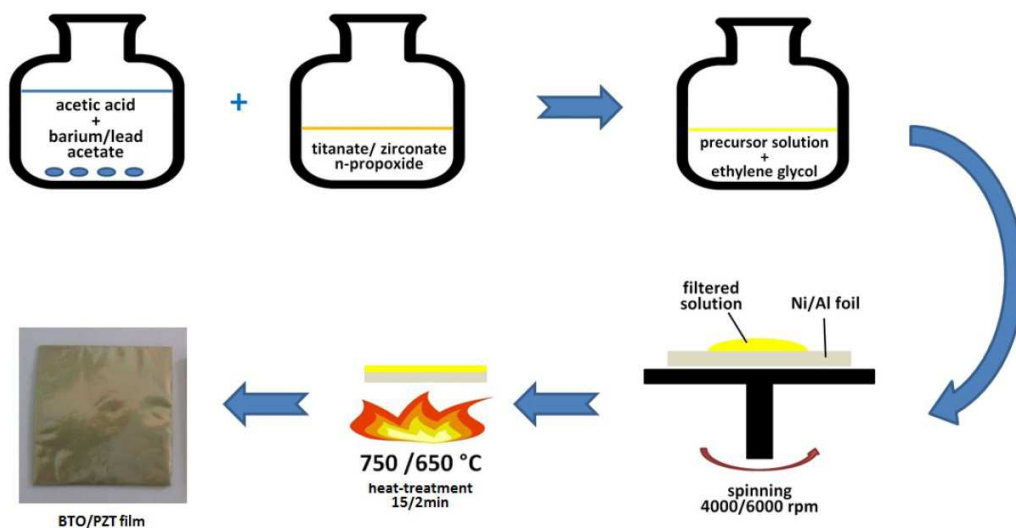


Figure 1. Scheme of Chemical Solution Deposition process used to obtain PZT and BTO thin films

The good crystallization of the piezoelectric films has been checked by X-ray diffraction (XRD) measurements (figure 2) and no pyrochlore phase has been detected (patterns have been obtained with a Bruker D8 diffractometer using Cu-K $\alpha$  radiation ( $\lambda = 1.5406 \text{ \AA}$ ) and scanning from  $2\theta = 20^\circ$  to  $2\theta = 60^\circ$  at  $0.03^\circ$  scan rate). However, NiO phase is observed in the case of the use of nickel substrates, especially in the pattern of Ni/BTO sample because the applied heat-treatment was the most important. NiO phase being not conductive, it would influence the quality of the electrical properties of the piezoelectric films.

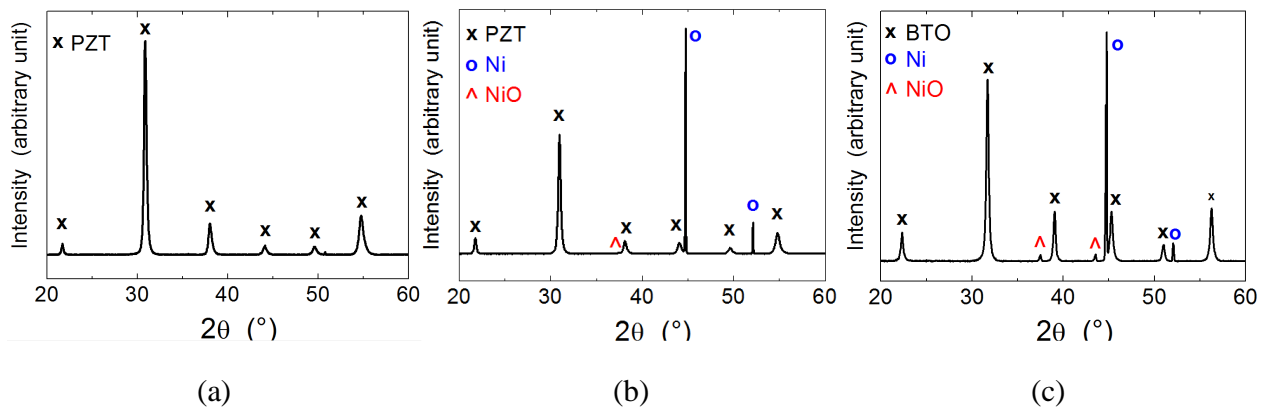


Figure 2. X-ray diffraction patterns of Al/PZT (a), Ni/PZT (b) and Ni/BTO (c) samples

### 3. Electrical properties

The permittivity and the dielectric losses have been measured by using a HP 4275A impedancemeter at 1 kHz. The P-E measurements have been done using a Sawyer-Tower circuit with a  $4.9 \mu\text{F}$  serial capacitor, and the applied sinusoidal electric field amplitude was tuned in order to obtain a same remanent polarization  $P_r$  for PZT films deposited onto aluminium and nickel foils. In table 2 have been reported the corresponding values for the different realized samples. In the case of PZT piezoelectric films, the low annealing temperature leads to low relative permittivity values (308 and 273 for PZT deposited onto Al and Ni foils respectively). However, the remanent polarization values are quite high at about  $25 \mu\text{C}/\text{cm}^2$ , which reveals an important ferroelectric behavior. By using Ni foil as substrate, the coercive field  $E_c$  value of PZT is decreased from 156 down to 80 kV/cm, which acts to an easier polarization of the PZT. Due to a higher heat-treatment of the BTO films, leading to an important oxidation of the Ni foil (observed in figure 2), the corresponding properties are weak compared to these of PZT films. An insulating NiO layer leads to a very low relative permittivity value of 62 and quite high coercive field value (287 kV/cm). Consequently, the polarization of the BTO is more difficult, resulting in a poor remanent polarization value ( $8.4 \mu\text{C}/\text{cm}^2$ ).

Table 2. Dielectric and ferroelectric properties of Al/PZT, Ni/PZT and Ni/BTO samples

sample	$\epsilon_r$	Tan $\delta$	$P_r$ ( $\mu\text{C}/\text{cm}^2$ )	$E_c$ (kV/cm)
Al/PZT/AL	308	0.019	25.0	156
Ni/PZT/Al	273	0.107	26.5	80
Ni/BTO/Al	62	0.052	8.4	287

#### 4. Energy harvesting measurements

To obtain flexible and waterproof generators, the prepared samples have been encapsulated in polyethylene terephthalate (PET, 150  $\mu\text{m}$ ) by a process of lamination as shown in figure 3.

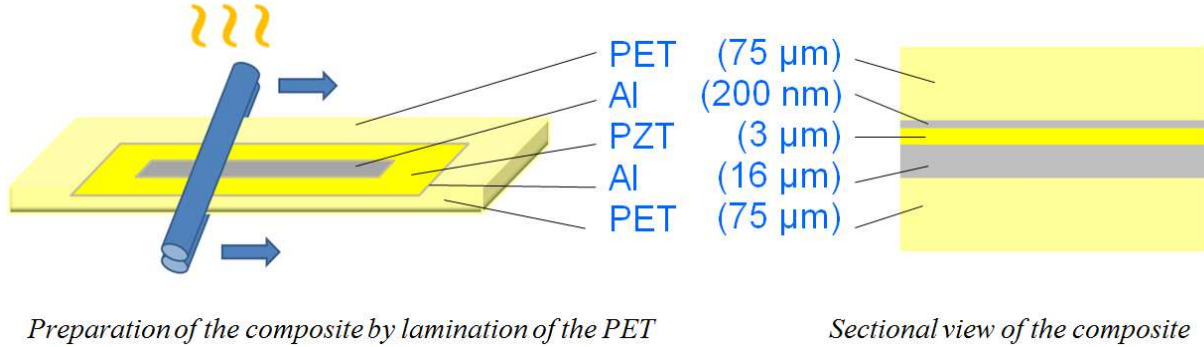


Figure 3. Scheme of the encapsulation process

The piezoelectric generators are inserted into a mechanical excitation device able to generate a variation of quasi-sinusoidal deformation of the flexible generator, leading to a quasi-sinusoidal signal observed on the oscilloscope  $u_R = U_R \cos(2\pi ft)$ . The measurement of the  $U_R$  amplitude of the voltage observed across the input impedance (1 M $\Omega$ ) of the oscilloscope makes it possible to calculate the amplitude of the short-circuit current  $I_0$ , the open-circuit voltage  $U_{oc}$  and the maximum power  $P_{max}$  thus delivered by the generator (eq. 1 to 4). Energy density has been calculated for each generator by taking into account the volume of the piezoelectric capacitor.

$$U_R = R \times I_R \quad (1) \quad I_R = \frac{I_0}{\sqrt{1 + R^2 C^2 \omega^2}} \quad (2) \quad P_{max} = I_0^2 / 4C\omega \quad (3) \quad U_{oc} = I_0 / C\omega \quad (4)$$

In table 3 are given the generators' properties obtained at a mechanical excitation of 1 Hz.

Table 3. Harvesting properties of Al/PZT, Ni/PZT and Ni/BTO generators

sample	$I_0$ (nA)	$U_{oc}$ (mV)	$P_{max}$ (nW)	$E_v$ ( $\mu\text{J}/\text{cm}^3$ )
Al/PZT/AL	455	411	47	84
Ni/PZT/Al	380	210	20	32
Ni/BTO/Al	14	51	0.18	0.2

Despite of its better ferroelectric properties, Ni/PZT/Al generator has lower harvesting properties than Al/PZT/Al generator, because of its lower piezoelectric current and higher capacitance at low frequency (250 nF versus 171 nF), which results in less than half harvested power. In the case of Ni/BTO/Al, the harvesting properties are poor compared to those of PZT generators, which is mainly due to the important oxidation of the Ni foil, as observed in the figure 2.

## 5. Conclusion

Flexible piezoelectric generators have been obtained using PZT and BTO thin films deposited by CSD onto thin aluminium and nickel foils. PZT generators exhibit interesting density of energy which allow their use in energy harvesting devices. At very low frequencies and because of its high heat-treatment, BTO generator exhibits poor harvesting properties. However, it can be used as sensor in applications where lead is prohibited.

## Acknowledgements

The authors would like to thank Jean-Emmanuel Lechêne from *Cookson SAS (Cholet, France)* for his receptiveness to supply the shadow masks required for electrode deposition. This work is supported by the French region *Pays de la Loire* through the 2014 07965 contract.

## References

- [1] D. Wang, M. Wright, N. K. Elumalai, and A. Uddin, « Stability of perovskite solar cells », *Sol. Energy Mater. Sol. Cells*, vol. 147, p. 255-275, 2016.
- [2] I. Sari, T. Balkan, and H. Kùlah, « An Electromagnetic Micro Power Generator for Low-Frequency Environmental Vibrations Based on the Frequency Upconversion Technique », *J. Microelectromechanical Syst.*, vol. 19, n° 1, p. 14-27, 2010.
- [3] F. Peano and T. Tambosso, « Design and optimization of a MEMS electret-based capacitive energy scavenger », *J. Microelectromechanical Syst.*, vol. 14, n° 3, p. 429-435, 2005.
- [4] G. Han and *al.*, « Stress-controlled  $\text{Pb}(\text{Zr}_{0.52}\text{Ti}_{0.48})\text{O}_3$  thick films by thermal expansion mismatch between substrate and  $\text{Pb}(\text{Zr}_{0.52}\text{Ti}_{0.48})\text{O}_3$  film », *J. Appl. Phys.*, vol. 110, n° 12, p. 124101, 2011.
- [5] R. Seveno and D. Averty, « Ultra light tunable capacitor based on PZT thin film deposited onto aluminium foil », *J. Sol-Gel Sci. Technol.*, vol. 68, n° 2, p. 175-179, 2013.
- [6] R. Seveno, P. Limousin, D. Averty, J.-L. Chartier, R. Le Bihan, and H. Gundel, « Preparation of multi-coating PZT thick films by sol-gel method onto stainless steel substrates », *J. Eur. Ceram. Soc.*, vol. 20, n° 12, p. 2025-2028, 2000.
- [7] G. Yi and M. Sayer, « Sol-Gel processing of Complex Oxide Films », *Ceram. Bull.*, vol. 70, n° 7, p. 1173-1179, 1991.

## Properties of CuInS<sub>2</sub>/TiO<sub>2</sub> Composite Solar Cell by CuInS<sub>2</sub> Nano-particles on TiO<sub>2</sub> thin film

\* Gye-Choon Park<sup>1)</sup>, Hyun-Su Jeong<sup>1)</sup>,

<sup>1</sup> Department of Electrical Engineering, Mokpo National University, Muan, Jeonnam 534-729, South Korea

**Key words:** I-III-VI<sub>2</sub> chalcopyrite semiconductor, photocatalyst, absorption layer,  
CuInS<sub>2</sub> / TiO<sub>2</sub> Composite solar cell,

**Abstract:** Copper Indium Disulfide (CuInS<sub>2</sub>) which is one of I-III-VI<sub>2</sub> chalcopyrite semiconductors possessing a direct band gap of 1.5 eV, has been attracted as a material for application of the photovoltaic solar cells. Titanium Oxide (TiO<sub>2</sub>) which is a semiconductor material with a large band gap of 3.2 eV, has been also widely used as a photocatalyst because of its high stability, favorable band gap energy, inexpensive cost and abundant availability. In this letter, CuInS<sub>2</sub> nano-particles deposited on TiO<sub>2</sub> porous film are applied for the use of the absorption layer of a solar cell, and the nano particles were prepared by using a method called the spray pyrolysis. Structural and optical properties of CuInS<sub>2</sub> nano-particles on TiO<sub>2</sub> were analyzed as a function of its composition ratios of Cu:In:S. Crystalline structure, surface morphology and crystalline size were also investigated by X-Ray Diffraction(XRD), Field Emission Scanning Electron Microscope(FESEM), and high-resolution TEM(HRTEM), respectively. On the other hand, optical property was characterized by an UV-Visible Spectrophotometer, and efficiency of solar cell was measured by solar simulator.

As a result, it was found that the size of CuInS<sub>2</sub> nano-particles, which was formed at ~350 °C, was smaller than 16 nm from HRTEM analyses, and it was identified that the CuInS<sub>2</sub> particle size was increased as increasing the heat-treatment temperature and time. However, as the size of CuInS<sub>2</sub> nano-particle becomes smaller, optical absorption edge of ternary compound film tends to move to the blue wavelength band. It turned out that the optical energy-band gap of the compound films was ranging from 1.45 eV to 1.70 eV, and the fabricated CuInS<sub>2</sub> / TiO<sub>2</sub> solar cell had an energy-conversion efficiency of 8.52%.

## 1. Introduction

I-III-VI<sub>2</sub> chalcopyrite semiconductor has been attracted considerably because of its excellent photovoltaic properties. Currently, the conversion efficiencies of such thin film solar cells fabricated based on I-III-VI<sub>2</sub> chalcopyrite compound semiconductor have been substantially enhanced [1,2].

It is well known that thin film of copper indium disulfide (CuInS<sub>2</sub>) exhibits the energy band gap of around 1.5 eV that is well matched to the spectrum of the solar energy. Furthermore, the absorbance coefficient of CuInS<sub>2</sub> is over 10<sup>5</sup> cm<sup>-1</sup>, so it is suitable for absorption layer of solar cell [3]. CuInS<sub>2</sub> has been also recognized as a promising material for solar energy application due to removal of the concern which is originated from the toxicity of Se[1].

In addition, nanostructured solar cells with large interfacial areas are expected to facilitate enhanced light absorption and charge separation that are the two critical mechanisms for a solar cell to effectively generate electrical energy. Recently, synthesis of various nanostructures applied for solar cells is steadily growing [4].

It was attempted that CuInS<sub>2</sub> nanoparticles was infiltrated into the porous TiO<sub>2</sub> layers by employing the atomic layer chemical vapor deposition and spray deposition as shown in Ref. by Z. Peng et al. [5].

In this work, CuInS<sub>2</sub> nanoparticles on TiO<sub>2</sub> porous film have been prepared by the spray pyrolysis which is applicable for the absorption layer of a thin film solar cell. Several characteristics including structural and optical properties of the CuInS<sub>2</sub> nanoparticles and conversion efficiency of CuInS<sub>2</sub> / TiO<sub>2</sub> composite solar cell were analyzed as a function of the heat-treatment condition and composition ratios of Cu:In:S.

## 2. Experiment

TiO<sub>2</sub> nanorods on a transparent FTO substrate were formed by using a hydrothermal method [2]. In order to deposit CuInS<sub>2</sub> into TiO<sub>2</sub> nanorods on FTO, SP(Spary Pyrolysis) method which is simple and low cost was utilized. For CuInS<sub>2</sub>, an aqueous solution containing copper chloride (CuCl<sub>2</sub>·2H<sub>2</sub>O), indium chloride (InCl<sub>3</sub>·4H<sub>2</sub>O), and thiourea (SC(NH<sub>2</sub>)<sub>2</sub>) was sprayed onto the substrate which was kept at a temperature of 300 ± 5 °C with a spray rate of 20 ml/min.

The thickness of the absorber layer was measured to be 0.6 mm which is prepared by spraying 375 ml of the solution. In order to increase the thickness of the absorber layer, two layers of CuInS<sub>2</sub> were deposited by separately spraying 375 ml and then 300 ml of the solution, reaching the absorber layer of 1.1 mm thick in total. Next, the cell was kept at the preparation temperature of 500 °C for 1 h to get better interface in the CuInS<sub>2</sub>- TiO<sub>2</sub> composite [1]. It is well known that Cu/In, S/Cu and In/S ratios of the films can be controlled by varying the molar concentrations of respective solutions [6]. In this experiment, the ratio of Cu/In was kept to be 1.0 and 1.2 while S/Cu ratio was kept to be 5 in the solution which is used in the fabrication step. The fabricated CuInS<sub>2</sub> thin films were named as C25-60, D25-60, E25-60, C25-60(S), D25-60(S) and E25-60(S) with the corresponding Cu:In:S composition ratios of 1.26:1:2.25, 0.97:1:1.96, 0.84:1:1.84, 1.13:1:2.13, 1.03:1:2.04 and 0.98:1:1.99, respectively. Finally, silver metal (45 nm thick) was then deposited as the top electrode using a vacuum evaporation technique to be an area of 0.009 cm<sup>2</sup>.

Structural analysis of the absorption layer was carried out using the Rigaku (D.Max.C) X-ray Diffractometer employing CuK $\alpha$  line and a Ni filter operated at 30 kV and 20 mA. Surface morphologies were investigated by Field Emission Scanning Electron Microscope(FESEM, JSM-6700 F, JEOL Co., Ltd.), Transmission Electron Microscopy(TEM, FEI Tecnai G2 30) and High-Resolution TEM(HRTEM, JEM-2100(UHR), JEOL Co., Ltd.).

The depth profile of the samples was obtained using an X-ray Photoelectron Spectroscopy (XPS) ULVAC-PHI unit (Model-ESCA 5600 CIM) employing an argon ion sputtering. Optical absorption characteristics were investigated using a UV-Vis-NIR Spectrophotometer (Hitachi U-3410 Model). Properties of solar cell measured by Solar simulator(XT-10, Spectrolab Co.) with Electronic load(D-1550, Spectrolab.co)

### 3. Results

#### 3-1. Structural Properties of $\text{TiO}_2$

Structural analysis reveals that the XRD patterns of the fabricated  $\text{TiO}_2$  thin films deposited on FTO substrates exhibit tetragonal rutile crystalline structure with miller index (101) at  $2\theta = 36.8^\circ$  and (002) at  $2\theta = 63.2^\circ$ . All the diffraction peaks of  $\text{TiO}_2$  thin films appeared upon FTO conductive glass agreed well with the tetragonal rutile phase [2].

#### 3-2. Structural Properties of $\text{CuInS}_2$

As depicted in figure 1, three additional peaks of  $\text{CuInS}_2$  over the XRD patterns of  $\text{TiO}_2$  porous film with heat-treatment temperature of  $500^\circ\text{C}$  for 1 h were located at  $2\theta = 27.9^\circ$ ,  $46.5^\circ$ , and  $55.1^\circ$  with the corresponding miller indices of (112), (204)/(220), and (116)/(312), respectively. The mean diameter of  $\text{CuInS}_2$  was calculated to be 8.3 nm which is calculated by the Scherrer equation;  $D = K\lambda / \beta \cos\theta$  ( $D$ : Crystallite size,  $K$ : Scherrer constant = 0.9,  $\lambda$ : Wavelength of X-ray,  $\beta$ : Integral breadth of peak (in radians  $2\theta$ ) located at an angle  $\theta$ ,  $\theta$ : Diffraction angle).

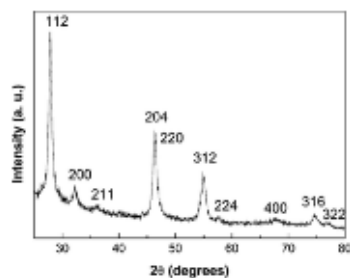


Figure 1. Measured XRD Patterns of  $\text{CuInS}_2$  nanoparticles.

#### 3-3. Surface Morphology of $\text{CuInS}_2$ - $\text{TiO}_2$

Figure 2(a) shows top view morphology of  $\text{CuInS}_2$ -  $\text{TiO}_2$  NRA (nanorod array) film taken from FESEM. Figure 2(b) shows top view morphology of  $\text{CuInS}_2$  nano-particles on  $\text{TiO}_2$  NRA film which was heat-treated for one hour at  $500^\circ\text{C}$ . It was calculated that the average diameter of  $\text{TiO}_2$  nanorods was to be  $\sim 100$  nm.

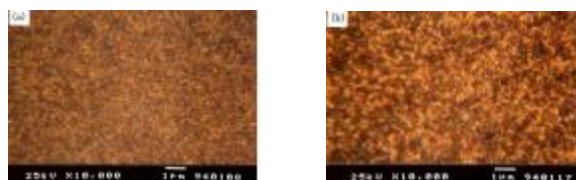


Figure 2. Top view images of  $\text{CuInS}_2$ -  $\text{TiO}_2$  composite prepared by FESEM; (a) in situ deposition of  $\text{CuInS}_2$  and (b) one hour heat-treatment after  $\text{CuInS}_2$  deposition.

In order to estimate the size of  $\text{CuInS}_2$  nano-particles, the edge side morphology of  $\text{TiO}_2$  nanorod was taken by HRTEM as shown in Figure 3. Figure 3(a) shows surface of pure  $\text{TiO}_2$  nanotube. And figure 3(b) shows that the average diameter of  $\text{CuInS}_2$  particles was ranging from 12 nm to 16 nm.

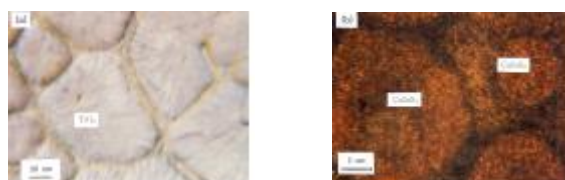


Figure 3. TEM images of (a) pure  $\text{TiO}_2$  nanotube and (b)  $\text{CuInS}_2$ -  $\text{TiO}_2$  nano tube composite.

#### 3-4. Optical Properties of $\text{CuInS}_2$

The light absorbance of sensitized  $\text{CuInS}_2$ -  $\text{TiO}_2$  thin film was extending to a region which is visible wavelength, and its absorbance tends to increase with the coating cycles. This is due to the increased amount of  $\text{CuInS}_2$  deposited on  $\text{TiO}_2$  by performing multiple coating cycles, corresponding to the substantial growth of the  $\text{CuInS}_2$  film. On the contrary, as the size of  $\text{CuInS}_2$  nano-particle becomes smaller, optical absorption edge of ternary compound film tends to move to the blue wavelength band.

The optical energy-band gap of the compound films is ranging from 1.45 eV to 1.70 eV.

#### 3-5 Efficiency of $\text{CuInS}_2$ / $\text{TiO}_2$ composite solar cell

Figure 4. showed I-V characteristic curves of the best fabricated  $\text{CuInS}_2$ /  $\text{TiO}_2$  solar cell by Xe lamp light intensity. At AM(Air Mass)1, the composite solar cell had an energy-conversion efficiency of 8.52% with  $V_{oc} = 580$  mV,  $I_{sc} = 30.6$  mA,  $FF = 0.72$ .

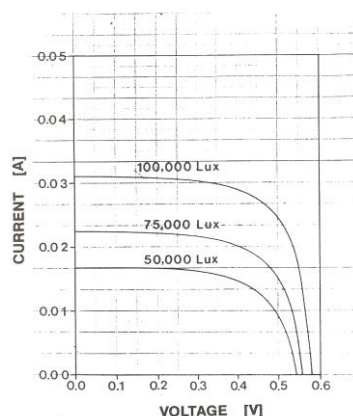


Figure 4. I-V curves of  $\text{CuInS}_2$ /  $\text{TiO}_2$  composite solar cell by light intensity.

#### 4. Conclusion

It was found that the size of CuInS<sub>2</sub> nano-particle, which was formed at around 300 ± 5 °C and heat-treated for one hour at 500 °C, was estimated to be less than 20nm, and the CuInS<sub>2</sub> particle size was increased with elevating the heat treatment parameters such as temperature and time. It was also identified that as decreasing the size of CuInS<sub>2</sub> nano-particle, optical absorption edge of ternary compound film tends to move to blue wavelength band region, and the corresponding optical energy-band gap of the compound films was ranging from 1.48 eV to 1.53 eV.

In conclusion, our experiment results indicate that the fabricated CuInS<sub>2</sub> / TiO<sub>2</sub> Solar cell had an energy-conversion efficiency of 8.52%, and the fabricated thin films can be applicable for an absorbing layer of the photovoltaic cells.

Acknowledgment : This work was supported by KEPCO Research Institute grant funded by Korea Electric Power Corporation(R16DA11)and KETEP(No.20164010100730)

#### References

1. M.V. Santhosh, D.R. Deepu, C.S. Kartha, K.R. Kumar and K.P. Vijayakumar, All sprayed ITO-free CuInS<sub>2</sub>/In<sub>2</sub>S<sub>3</sub> solar cells, *Solar Energy*, 108(2014), 508-514.
2. B. Liu and E.S. Aydil, Growth of Oriented Single-Crystalline Rutile TiO<sub>2</sub> Nanorods on Transparent Conducting Substrates for Dye-Sensitized Solar Cells, *J. AM. CHEM. SOC.*, 131(2009), 3895-3990.
3. J.J. Wu, W.T. Jiang and W.P. Liao, CuInS<sub>2</sub> nanotube array on indium tin oxide: synthesis and photoelectrochemical properties, *Chem Commun.*, 45(2010), 5885-5887.
4. M.M. Kamazan, M. S. Niasari and H. Emadi, Preparation of stoichiometric CuInS<sub>2</sub> nanostructures by ultrasonic method, *Micro & Nano Letters*, 7(9), (2012), 896-900.
5. Z. Peng, Y. Liu, W. Shu, K. Chen and W. Chen, Synthesis of Various Sized CuInS<sub>2</sub> Quantum Dots and Their Photovoltaic Properties as Sensitizers for TiO<sub>2</sub> Photoanodes, *Eur. J. Inorg. Chem.* 2012, 5239-5244.
6. G.C. Park, H.D. Chung, C.D. Kim, H.R. Park, W.J. Jeong, J.U. Kim, H.B. Gu and K.S. Lee, Photovoltaic Characteristics of CuInS<sub>2</sub>/CdS Solar Cell by EBE, *Solar Energy Materials and solar Cells*, 49(1997), 365-374.

# Adsorption of indium ions from aqueous solution onto a bentonite

N. Homhuan<sup>1</sup>, S. Bureekaew<sup>2</sup> and M. Ogawa<sup>2\*</sup>

<sup>1</sup> School of Molecular science and engineering, Vidyasirimedhi Institute of Science and Technology, 555 Moo 1, Payupnai, Wangchan, Rayong 21210, Thailand

<sup>2</sup> School of Energy science and engineering, Vidyasirimedhi Institute of Science and Technology, 555 Moo 1, Payupnai, Wangchan, Rayong 21210, Rayong, Thailand

## Abstract

The concentration of indium<sup>3+</sup>; In(III) from aqueous solutions by the adsorption on a bentonite was investigated. Indium was selected as the target for the present study, because it is a rare and valuable element and is used in a wide range of industrial applications. A bentonite (code name SN-1, obtained from Thai Nippon Chemical Co.) was used as the adsorbent. The In(III) adsorption isotherm onto the bentonite was classified as type H, which indicated the high affinity of In(III) and the bentonite. The maximum adsorbed amount of In(III) on the bentonite was 0.35 mmol/g clay, which was determined by the Langmuir plot of the adsorption isotherm. The reactions took only 10 minutes, which is an advantage of the present method using the bentonite for the practical application of In(III) recovery.

## 1. Introduction

The adsorption (ion exchange) of ions onto solids is a way for the concentration of toxic and noble ions from aqueous environments. In addition to the application for the recovery of target metal ions from environments, the adsorption was regarded as a way to prepare functional hybrids based on layered materials.<sup>1-3</sup> In this research, indium was selected as the target metal, because the industrial application of In(III) is widespread and there is a demand for the efficient In(III) recovery from various environments.<sup>4</sup> The toxicity of the indium compounds<sup>5</sup> make the In(III) collection from the environment more important. In the present study, the adsorption of In(III) onto bentonite was investigated. Bentonites are naturally occurring materials with a wide range of application, and has been used adsorbents effective to the cationic species.<sup>2</sup>

## 2. Experimental

A bentonite (SN-1, obtained from Thai Nippon Chemical Co.) was used as the adsorbent without further purification. Adsorption of In(III) onto bentonite was examined by the following procedure; bentonite (0.1 g) was mixed with an aqueous solution (50 mL) of In(III) chloride and the mixture was allowed to react for 10 min at room temperature. After the centrifugation at 4,000 rpm for 5 min, the resulting precipitate was dried at room temperature in a vacuum oven for 1 day. The concentration of In(III) in the supernatant was determined by ICP. The solid samples were characterized by X-ray powder diffraction patterns and the chemical composition was determined by ICP analysis of the supernatant.

## 3. Results and discussion

The adsorption isotherm of In(III) onto bentonite from aqueous solutions is shown in Fig. 1. The isotherm was classified as type H according to the classification by Giles *et al.*<sup>6</sup>, that showed the high affinity between In(III) and the bentonite. In order to avoid the precipitation of basic salts of metal ions, the solution is recommended to be maintained in slightly acidic during the ion exchange reactions. In the present study, the pH of the initial solution of indium chloride was in the range of 3.5 – 4.0, and it became 3.0 – 4.5 during the reaction as a result of the ion exchange of In(III) with the interlayer cation of bentonite (mainly sodium or calcium). The pH values were not high enough for In(III) to precipitate as hydroxides, so that the cation exchange occurred preferentially.

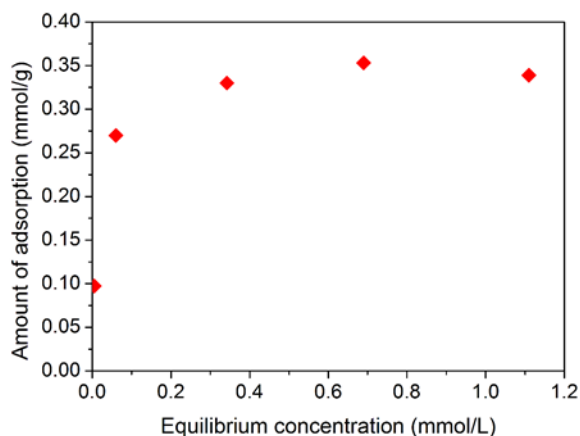


**Fig. 1.** The adsorption isotherm of In (III) onto bentonite

The adsorption of In(III) to bentonite was evaluated by Langmuir plot of the adsorption isotherm as shown in Fig. 2. The Langmuir plot fitted very well with the high correlation coefficient ( $R^2 = 0.9990$ ) for the adsorption of In(III) examined in the present study. The Langmuir isotherm confirmed the interactions between In(III) cation and negative charge of layered silicate to form an ordered monolayer of In(III). The Langmuir parameters of the adsorption of In(III) onto the bentonite were determined to be  $q_m = 0.35$  mmol/g and  $K_L = 81$  L/mmol.

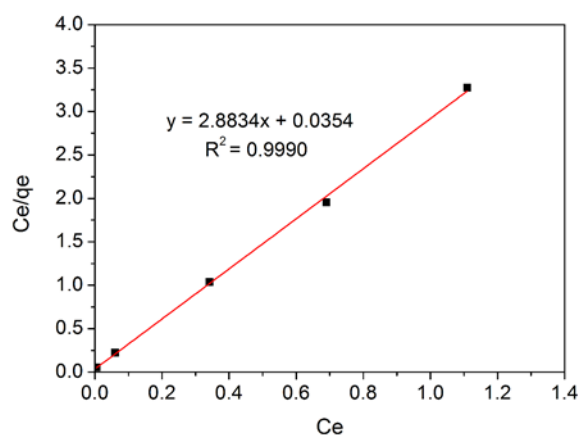


**Fig. 2.** Langmuir plot of the adsorption of In(III) onto bentonite from aqueous solutions.

The XRD patterns of the samples after the adsorption of In(III) are shown in Fig. 3, together with that of the original bentonite. The basal spacing (1.52 nm, which is a typical value of calcium-type bentonite) of the bentonite, decreased after the ion exchange with In (III) to be ca. 1.41 nm. The change in the basal spacing

reflected the ion exchange and the difference in the hydration level between Ca- and In(III)-bentonites.

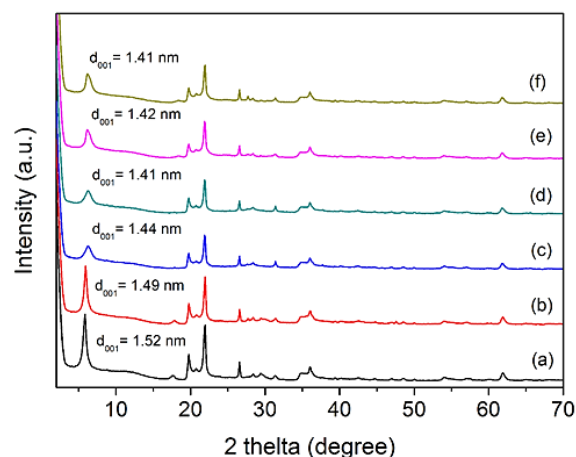


**Fig. 3.** X-Ray powder diffraction patterns of bentonite (a) before and (b-f) after the reactions with indium chloride (using the solutions of the concentration of 0.2 (b), 0.6 (c), 0.10 (d), 0.14 (e) and 0.18 mM (f)).

#### 4. Conclusions

Bentonite was used for the concentration of In(III) from aqueous solutions. The adsorption capacity (0.35 mmol/g of bentonite), short reaction time (10 min at room temperature), easy separation of adsorbent by centrifugation (or filtration) were ideal for the In(III) recovery from aqueous environments.

#### References

1. M. Ogawa, K. Saito and M. Sohmiya, *Dalton Trans.*, 2014, **43**, 10340–10354.
2. T. Okada, Y. Ide and M. Ogawa, *Chem. Asian J.*, 2012, **7**, 1980-1992.
3. T. Okada, Y. Seki, M. Ogawa, *J. Nanosci. Nanotechnol.* 2014, **14**, 2121-2134.
4. A. M. Alfantazi and R. R. Moskalyk, *Miner. Eng.*, 2003, **16**, 687–694.
5. A. Tanaka, M. Hirata, Y. Kiyohara, M. Nakano, K. Omae, M. Shiratani and K. Koga, *Thin Solid Films*, 2010, **518**, 2934–2936.
6. C. H. Giles, D. Smith and A. Huitson, *J. Colloid Interface Sci.*, 1974, **47**, 755-765.

# Helicity dependent photocurrents in ABA- and ABC-stacked trilayer graphene

B. Cao<sup>1</sup>, X. Qian<sup>2</sup>, M. Eginligil<sup>2\*</sup>, T. Yu<sup>1</sup>

<sup>1</sup> Division of Physics and Applied Physics, School of Physical and Mathematical Sciences, Nanyang Technological University, 637371, Singapore

<sup>2</sup> Key Laboratory of Flexible Electronics (KLOFE) & Institute of Advanced Materials (IAM), Jiangsu National Synergetic Innovation Center for Advanced Materials (SICAM), Nanjing Tech University (NanjingTech), 30 South Puzhu Road, Nanjing 211816, China

\* email: [iameginligil@njtech.edu.cn](mailto:iameginligil@njtech.edu.cn)

## Abstract:

We present our recent photocurrent studies of three layer (trilayer) graphene upon excitation by elliptically polarized light. We measured the photocurrent of two devices with different stacking, namely ABA- (which consists of one single layer graphene-like and another bilayer graphene-like subband) and ABC-stacked (approximately cubic band dispersion and band gap opening by gating). The photocurrent of these devices showed strong dependence on angle of photon polarization. Photocurrent contributions due to the linear photon drag effect and the circular photogalvanic effect were extracted by fitting the data to a phenomenological photocurrent formula. By varying the gate voltage, we tuned the devices from p-type at zero gate voltage to n-type at 40 V gate voltage. In the case of the ABC-stacked device, the difference between the values of the circular photogalvanic current for p-type and n-type was 4 times larger than that of the ABA-stacked device. This observation was discussed in terms of inversion symmetry and band gap opening in ABC-stacked.

**Keywords:** graphene photoresponse, circular photogalvanic effect, trilayer graphene.

## Introduction:

Helicity dependent photocurrent (PC) in single layer graphene (SLG) is the electric current generated by elliptically polarized light which is obliquely incident on to a sample plane. The helicity dependent PC of an n-type SLG was measured and the PC contributions were extracted by using a phenomenological PC formula.  $J = C_1 \sin(2\varphi) + L_1 \sin(4\varphi) + L_2 \cos(4\varphi) + D$ , where  $\varphi$  is the angle of photon polarization;  $C_1$  and  $L_1$  are the PC contributions due to the circular and linear photogalvanic effect (CPGE – LPGE), respectively;  $L_2$  is the linear photon

drag effect (LPDE) and  $D$  is the polarization independent PC contribution [1]. The PC due to the LPDE is simply related to light momentum transfer on to the sample; while the PC due to the CPGE is due to the interaction of electromagnetic wave with the sample on a substrate, therefore the substrate and the point group symmetry of the sample is crucial for the existence of such a PC contribution. In graphene, the CPGE is allowed.

Unlike SLG, a band gap can open in bilayer graphene (BLG) by applying gate voltage. The most stable structure of BLG is AB-stacked and there is an inversion symmetry breaking in BLG. The PC of BLG and SLG as a function of light helicity and carrier density (by applying back gate voltage ( $V_{bg}$ )) was recently studied [2]. The PC due to the CPGE in BLG was expected to be larger than SLG. However, both the PCs due to the LPDE and the CPGE showed features in common with SLG, except an anomaly observed in BLG which has a  $\cos(\varphi)$  dependence.

Addition of one more layer on to BLG leads to trilayer graphene (TLG) which can be either ABA-stacked or ABC-stacked. The ABA-stacked TLG consists of SLG-like and BLG-like subbands and has broken inversion symmetry [3]. On the other hand, the band dispersion of ABC-stacked TLG is approximately cubic, the inversion symmetry is restored compared to AB-stacked BLG and it has a band gap opening by gating, as shown by electrical transport measurements [4, 5].

## Method and measurements:

We measured the PC of ABA- and ABC-stacked TLG samples fabricated into FET devices. An experimental setup similar to our pre-

vious work [6] has been used. The oblique angle was kept at  $45^\circ$ . Initially we didn't apply any  $V_{bg}$ . Figure 1 shows the PC of the ABA-stacked TLG as a function of angle of photon polarization,  $\varphi$  for  $V_{bg} = 0$ . The data were fit to the phenomenological PC formula from which the PC contributions  $C_1$ ,  $L_1$ (negligible),  $L_2$ , and D were extracted. Similarly, the ABC-stacked TLG device was measured and it qualitatively showed similar behavior.

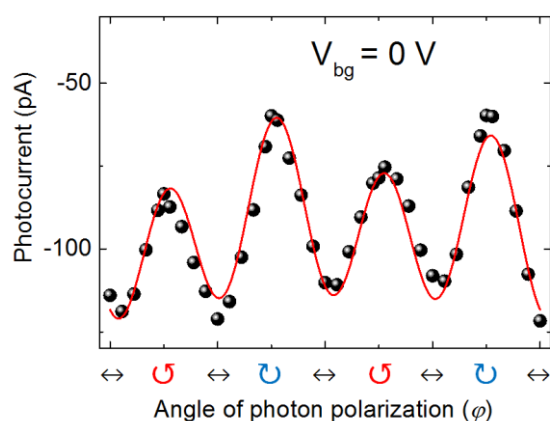


**Figure 1:** Light helicity dependent photocurrent in ABA-stacked TLG sample. Black dots are the data, the red curve is the fit by the phenomenological formula.

### Results and discussion:

From the fitting formula we determined the major PC components  $C_1$ , the CPGE PC and  $L_2$  the LPDE PC, at  $V_{bg} = 0$ , from Fig. 1. At  $V_{bg} = 0$ , the ABA-stacked TLG device is p-type, and the determined values are tabulated in Table 1. Then, by making  $V_{bg} = +40$  V, we tuned the device into n-type by crossing the charge neutrality point at  $+28$  V and similarly we extracted  $C_1$  and  $L_2$  from the same PC formula. By following the same procedure, we tuned the ABC-stacked TLG device to n-type at  $V_{bg} = +40$  V, which was p-type at  $V_{bg} = 0$  by crossing the charge neutrality point at  $+18$  V. Then, we determined  $C_1$  and  $L_2$  for both p-type and n-type ABC-stacked TLG device in Table 2.

ABA-stacked	CPGE PC (pA)	LPDE PC (pA)
p-type	-3	-21
n-type	0	11

**Table 1.** The major PC contributions of ABA-stacked TLG device in p-type regime at  $V_{bg} = 0$  V and n-type regime at  $V_{bg} = +40$  V.

While the LPDE PC in TLG samples are similar as seen Tables 1 and 2; a large change in the CPGE PC of ABC-stacked TLG ( $\sim 12.5$  pA) was observed between n-type and p-type unlike the ABA-stacked TLG ( $\sim 3$  pA). It is important to note that similar PC due to LPDE were obtained for SLG and BLG. However the variation in the CPGE PC in ABC-stacked TLG is much larger than SLG, BLG and ABA-stacked TLG (at least 4 times). The possible reason could be due to the band gap opening in ABC-stacked TLG while it is an inversion symmetric system.

ABC-stacked	CPGE PC (pA)	LPDE PC (pA)
p-type	-9	-20
n-type	3.5	6

**Table 2.** The major PC contributions of ABC-stacked TLG device in p-type regime at  $V_{bg} = 0$  V and n-type regime at  $V_{bg} = +40$  V.

### Conclusion:

We measured helicity dependent PC of ABA- and ABC-stacked TLG FET devices by varying the angle of photon polarization at an oblique angle. We fit these data to a phenomenological PC formula from which we determined the major PC contributions such as the CPGE and LPDE PCs. By turning the devices from p-type to n-type we observed the changes in these PC contributions. While the LPDE PCs yields similar dependency, the CPGE PC for ABC-stacked TLG showed a clear tuneability, unlike ABA-stacked device, which could be useful for graphene optoelectronic applications. Further experimental and theoretical work is underway to elaborate this interesting observation.

### Acknowledgements:

This work is supported in part by National Synergetic Innovation Center for Advanced Materials (SICAM), the start-up fund by Nanjing Tech University, and Jiangsu 100 Talent. Prof. Ting Yu acknowledges the funds by Singapore Ministry of Education under MOE2015-T1-001-065 and MOE2015-T1-002-126.

### References:

- Jiang C. et al. (2011) Helicity-dependent photocurrents in graphene layers excited by midinfrared radiation of a  $CO_2$  laser, *Phys. Rev. B*, **84**, 125429.

2. Eginligil M. et al. (2017) to be submitted.
3. Lui C. H., Li Z., Mak K. F., Cappelluti E., Heinz T. F. (2011) Observation of an electrically tunable band gap in trilayer graphene, *Nat. Phys.*, **7**, 944-948.
4. Bao W., et al. (2011) Stacking-dependent band gap and quantum transport in trilayer graphene, *Nat. Phys.*, **7**, 948-952.
5. Jhang S. H., et al. (2011) Stacking order dependent transport properties of trilayer graphene, *Phys. Rev. B*, **84**, 161408(R).
6. Eginligil M., Cao B., Wang Z., Shen X., Cong C., Shang J., Soci C., Yu T. (2015) Dichroic spin-valley photocurrent in monolayer molybdenum disulphide, *Nat. Commun.* **6**, 7636.